The Astrophysical Journal, 998:54 (37pp), 2026 February 10 https://doi.org/10.3847/1538-4357/ae2be8

Spectroscopic Follow-up of Gaia Alerted Young Stellar Object Variables: The Large Binocular Telescope View

Teresa Giannini[1], Manuele Gangi[2], Fernando Cruz-Sáenz de Miera[3,4], Brunella Nisini[1], Máté Szilágyi[4], Katia Biazzo[1], Ágnes Kóspál[4,5], Péter Ábrahám[4,5], Simone Antoniucci[1], Roberta Carini[1], Eleonora Fiorellino[6,7], Adriana Gargiulo[8], Ester Marini[1], Zsófia Nagy[4], Maria Gabriela Navarro[1], and Fabrizio Vitali[1]
[1] INAF—Osservatorio Astronomico di Roma, Via di Frascati, 33, 00078, Monte Porzio Catone, Italy; teresa.giannini@inaf.it
[2] ASI, Italian Space Agency, Via del Politecnico Snc., 00133 Rome, Italy
[3] Institut de Recherche en Astrophysique et Planétologie, Université de Toulouse, UT3-PS, OMP, CNRS, 9 Av. du Colonel Roche, 31028, Toulouse Cedex 4, France
[4] HUN-REN Research Centre for Astronomy and Earth Sciences, Konkoly Observatory, MTA Centre of Excellence, Konkoly Thege Miklós út 15-17, H-1121 Budapest, Hungary
[5] ELTE Eötvös Loránd University, Institute of Physics and Astronomy, Pázmány Péter sétány 1A, Budapest 1117, Hungary
[6] Alma Mater Studiorum—Universitá di Bologna, Dipartimento di Fisica e Astronomia "Augusto Righi," Via Gobetti 93/2, I-40129 Bologna, Italy
[7] INAF—Osservatorio Astronomico di Trieste, via Tiepolo 11, I-34143 Trieste, Italy
[8] INAF—Istituto di Astrofisica Spaziale e Fisica Cosmica Milano, Via A. Corti 12, 20133 Milano, Italy
Received 2025 October 6; revised 2025 December 1; accepted 2025 December 9; published 2026 February 3

Abstract

We analyzed optical/near-IR Large Binocular Telescope spectra of 16 sources alerted by Gaia between 2021 and 2024 due to significant photometric variability. Half of the spectra were taken during quiescence and the rest during a burst or at intermediate brightness. Our analysis of their 10 yr light curves and photometric/spectroscopic features provides evidence that all 16 sources are accreting young stellar objects (YSOs). One object, Gaia23bab, is a known EXor source. Other light curves either have peaks over a stable baseline or significant variability throughout the entire observation period, suggesting multiple contributing processes. All spectra exhibit emission lines from accretion columns, and over half of them show atomic forbidden lines as signatures of outflowing gas. We determined stellar parameters, accretion luminosity ($L_{\rm acc}$), and mass accretion rate ($\dot{M}_{\rm acc}$) at different brightness phases. Only two sources showed variability primarily due to extinction. During quiescence, our sources exhibit $L_{\rm acc}$ and $\dot{M}_{\rm acc}$ values typical of T Tauri and Herbig Ae/Be (HAeBe) sources, supporting the hypothesis that any YSO may undergo episodic accretion. In bursts, the $L_{\rm acc}$ and $\dot{M}_{\rm acc}$ of sources with photometric variations exceeding 2 mag follow a shallower relation with stellar luminosity and mass, typical of known EXor sources. This group includes one Class I, one flat-spectrum, and two Class II sources. Notably, the other Class I source, Gaia24beh, shows an $L_{\rm acc}$ value about 10 times higher than typical EXor bursts of the same mass. In the other cases, $L_{\rm acc}$ and $\dot{M}_{\rm acc}$ align with variability seen in T Tauri and HAeBe sources.

Unified Astronomy Thesaurus concepts: Eruptive variable stars (476); Stellar accretion (1578); Pre-main sequence stars (1290); Star formation (1569)

1. Introduction

Variability is a defining feature of accreting young stellar objects (YSOs). Around 50% of YSOs are subject to short-term events, occurring on minute-to-day timescales with photometric oscillations of a few tenths of a magnitude (e.g., S. T. Megeath et al. 2012). This type of variability is typically associated with stellar activity such as surface spots, stellar flares, and coronal mass ejections.

Superimposed on this, longer-term variability, ranging from months to years and even centuries, is sometimes observed (W. J. Fischer et al. 2023). This long-term variability is typically induced by changes in extinction caused by inner-disk warps and clumps (e.g., G. M. Kennedy et al. 2017), or by abrupt variations in the mass accretion rate ($\dot{M}_{\rm acc}$) from typical values of 10^{-10}–10^{-8} $M_\odot\,{\rm yr}^{-1}$ to 10^{-6}–10^{-4} $M_\odot\,{\rm yr}^{-1}$ (L. Hartmann & S. J. Kenyon 1996; M. Audard et al. 2014). Sources exhibiting this latter class of variability are known as eruptive young stars (EYs).

EYs encompass sources with diverse photometric and spectroscopic features. The original classification (G. H. Herbig 1977, 1989) was based on optical observations and identified two classes: FU Ori-type objects (FUors), which brighten by 4−5 mag for decades or longer and exhibit spectra with absorption lines, and EX Lupi-type objects (EXors), which show repetitive bursts of 1−3 mag lasting from months to one year, with spectra displaying emission lines. Until about 20 yr ago, only a few dozen eruptive variables were known. In the last decade, photometric monitoring from surveys like Gaia[9] (Gaia Collaboration et al. 2016), Zwicky Transient Facility[10] (ZTF; E. C. Bellm et al. 2019), Pan-STARSS[11] (K. C. Chambers et al. 2016), ASAS-SN[12] (T. Jayasinghe et al. 2018), VISTA Variables in the Via Lactea/VVVX[13] (D. Minniti et al. 2010), and AllWISE/NEOWISE[14] (A. Mainzer et al. 2011; E. L. Wright et al. 2010) has significantly increased both the observational cadence and the

[9] https://www.esa.int/Science_Exploration/Space_Science/Gaia
[10] https://www.ztf.caltech.edu/
[11] https://outerspace.stsci.edu/display/PANSTARRS/
[12] https:www.astronomy.ohio-state.edu/asassn/
[13] https://vvvsurvey.org/
[14] https://www.nasa.gov/mission_pages/WISE/main/index.html

covered wavelength range. This has led to a more than threefold increase in the number of EYs, with hundreds of new candidates. This progress has facilitated the discovery of EYs at early evolutionary stages (e.g., Y.-H. Lee et al. 2021; E. J. Safron et al. 2015; W. Zakri et al. 2022) and across a wide mass range extending to high-mass protostars (e.g., A. Caratti o Garatti et al. 2017; T. R. Hunter et al. 2017). C. Aspin & B. Reipurth (2003), and, more recently, M. S. Connelley & B. Reipurth (2018) and C. Contreras-Peña et al. (2025a) have defined, together with FUors and EXors, three more EYs subclasses: FUor-like, namely, objects that share with FUors the same absorption features but where no outburst has been observed, peculiar/V1647Ori-like/MNors sources, which appear intermediate between FUors and EXors, and periodic objects, showing a quasiperiodic variability.

The rising number of discovered EYs has increased the interest of the community in the role that outbursts may have on the formation and evolution of the stellar-disk system. Outbursts, for instance, can modify the chemistry of disks and envelopes and influence the planet formation process. The elevated temperatures they induce in the disk can temporarily shift, at larger disk radii, the location of various ice snow lines (A. Hubbard 2017). Additionally, outbursts are believed to contribute over 20% of a star's total mass (W. J. Fischer et al. 2019; F. Cruz-Sáenz de Miera et al. 2023; T. Giannini et al. 2024) and significantly impact the stellar luminosity. They also, at least partially, account for the widespread observed relation between accretion and stellar luminosity (W. J. Fischer et al. 2023).

The wide variety of photometric variability described above makes it unlikely that a single cause can be responsible for the observed outbursts. Indeed, from the theoretical point of view, a large number of mechanisms have been proposed as the basis for outburst triggering, essentially falling into two main schools of thought: "internal" and "external" triggering. Internal triggering mechanisms involve processes within the star–disk system, such as: thermal viscous instability (K. R. Bell & D. N. C. Lin 1994; S. Nayakshin et al. 2024), gravitational and magnetorotational instabilities (Z. Zhu et al. 2009; J. Bae et al. 2014; K. Kadam et al. 2020), disk fragmentation (E. I. Vorobyov & S. Basu 2015), planet–disk interaction (G. Lodato & C. J. Clarke 2004), and extreme evaporation of planets in hot thermally unstable protoplanetary disks (S. Nayakshin et al. 2023). External triggering mechanisms include: binary interactions (I. Bonnell & P. Bastien 1992), capture of fragments of the native molecular cloud (C. P. Dullemond et al. 2019), and collisions of disks in stellar flybys (E. M. A. Borchert et al. 2022; R. Dong et al. 2022).

While significant progress has been made in photometric observations and modeling, spectroscopic monitoring has not developed at a similar level (e.g., M. S. Connelley & B. Reipurth 2018; T. Giannini et al. 2022; C. Contreras-Peña et al. 2025b), despite being crucial for distinguishing between various types of variability and, consequently, for discovering genuine young eruptive variables. In the last decade, the Gaia Photometric Science Alert system[15] (S. T. Hodgkin et al. 2021) has provided alerts of significant photometric variability for about 850 YSOs or candidates. In-depth studies of the photometric and spectroscopic characteritics of Gaia-alerted sources have led to the identification of a number of new FUors (Gaia17bpi, L. A. Hillenbrand et al. 2018; Gaia18dvy, E. Szegedi-Elek et al. 2020; and Gaia21elv, Z. Nagy et al. 2023) and EXors (Gaia18dvz, K. W. Hodapp et al. 2019; Gaia20eae, F. Cruz-Sáenz de Miera et al. 2022; A. Ghosh et al. 2022; Gaia19fct, S. Park et al. 2022; Gaia23bab, T. Giannini et al. 2024; Z. Nagy et al. 2025) as well as sources belonging to new subclasses (Gaia19ajj, L. A. Hillenbrand et al. 2019; Gaia19bey, K. W. Hodapp et al. 2020; Gaia21bty, M. Siwak et al. 2023; Gaia18cjb, E. Fiorellino et al. 2024).

This paper is aimed at examining the eruptive accretion phenomenon from a more statistical perspective, being based on Large Binocular Telescope (LBT) spectroscopic observations of a sample of 16 Gaia-alerted sources. Rather than focusing on an in-depth analysis of individual sources, our goal is to define the key photometric and spectroscopic characteristics that identify eruptive variables, specifically their light-curve features and their accretion luminosity and mass accretion rate. Our paper is organized as follows: Section 2 presents our sample of Gaia-alerted sources and the all-sky surveys used for the photometric analysis; Section 3 describes the observations and data reduction procedures; Section 4 presents the multiwavelength light curves; Section 5 illustrates the methods adopted to compute the extinction in each source; Section 6 describes the spectral energy distribution (SED) of our sources, along with an analysis of the optical and IR colors; Section 7 presents the spectra and the determination of the stellar and accretion parameters; Section 8 discusses our results, and Section 9 presents the conclusions. Additionally, in Appendix A, we give notes on the individual sources, and in Appendix B, we present the photometric data. Finally, in Appendices C and D, the observed spectra and the tables of the line fluxes are shown.

2. The Sample

Our initial sample was derived from the publicly available Gaia alerts catalog, specifically selecting sources classified[16] as "YSO" or "YSO candidate" (S. T. Hodgkin et al. 2021). While this selection increases the probability of focusing on genuine YSOs, it is important to note that a substantial number of potentially outbursting YSOs were likely excluded, as approximately 75% of Gaia alerts currently lack a definitive classification. From the initial set of about 850 objects, we further selected sources that showed a significant brightening ($\sim$1−2 mag) in the G band during the period between 2021 and 2024. To ensure they are readily observable with the LBT, we further required them to be visible from the Northern hemisphere and have an average G magnitude $\lesssim$17.5. Approximately 60 objects met these criteria. Here we present a study of a subsample comprising 16 of these objects. Future observations are planned to extend the sample and will be presented in forthcoming papers.

In Table 1 we present our sample. Along with the coordinates, location, and distance (Section 2.2), we include the Gaia RUWE[17] parameter, the classification (YSO or YSO candidate) obtained from the Gaia Alert Index, and the name provided in the Simbad[18] database. Out of the eight YSO

[15] https://gsaweb.ast.cam.ac.uk/alerts/alertsindex

[16] We considered both the Gaia "class" and "comment" columns in the Gaia Alert Index.

[17] The Gaia RUWE (renormalized unit weight error) parameter is a powerful indicator of multiplicity. Typically, it approximates unity for well-behaved individual sources.

[18] https://simbad.cds.unistra.fr/simbad/sim-fid

Table 1
Sample

ID	Source	R.A.(J2000.0) (h:m:s)	Decl. (J2000.0) (deg:arcmin: arcsec)	Region	Distance (pc)	RUWE	Gaia Classification[a]	Simbad Name
1	Gaia21bkw	03:28:56.97	+31:16:22.12	NGC 1333	265 (a)	1.04	YSO	2MASS J03285694+3116222
2	Gaia22efa	04:30:37.49	+35:50:31.56	Auriga–California	532	2.29	YSO-c	AKARI-IRC-V1 J0430375 +355031
3	Gaia22bvi	04:56:57.02	+51:30:50.40	L1438	209 (b)	2.16	YSO	V347 Aur
4	Gaia22ehn	04:33:19.09	+22:46:33.71	LDN 1536	152 (c)	4.82	YSO-c	IRAS 04303+2240
5	Gaia22dbd	05:31:55.50	−02:52:19.27	Orion	345	1.17	YSO	UCAC4 436-010349
6	Gaia21arv	05:35:05.62	−05:29:22.38	Orion	390	1.09	YSO	V407 Ori
7	Gaia23bri	05:41:13.79	+27:39:38.45	⋯	1586	1.04	YSO-c	2MASS J05411378+2739385
8	Gaia21ebu	06:31:36.86	+04:51:04.32	Rosette nebula	1383	1.62	YSO	V546 Mon
9	Gaia21aul	18:30:06.18	+00:42:33.30	Serpens	379	2.74	YSO	IRAS 18275+0040
10	Gaia23bab	19:04:26.68	+04:23:57.37	G38.3-0.9	900 (d)	1.00	YSO-c	2MASS J19042667+0423575
11	Gaia23dhi	19:35:56.88	+16:28:23.38	⋯	2735	1.02	YSO-c	ZTF J193556.88+162823.4
12	Gaia24afw	19:43:44.62	+23:14:44.66	⋯	2150	2.51	YSO-c	2MASS J19434462+2314447
13	Gaia21faq	20:41:20.62	+39:29:32.06	Cygnus X	1190	6.42	YSO-c	[KMH2014] J204120.63 +392931.95
14	Gaia24beh	20:50:50.39	+44:50:11.44	Cygnus	741	1.07	YSO	[KW97] 50-20
15	Gaia21fji	21:03:58.14	+50:14:40.20	L998	225/626 (c)	9.04	YSO-c	HBC727
16	Gaia21csu	23:02:44.39	+61:39:31.86	LDN 1218	834	1.45	YSO	ZTF J230247.47+613919.1

Note.
[a] YSO-c stands for "YSO candidate."
References. (a) E. Fiorellino et al. (2021); (b) S. E. Dahm & L. A. Hillenbrand (2020); (c) Z. Nagy et al. (2025, in preparation); (d) T. Giannini et al. (2024).

Table 2
Stellar Parameters Retrieved from the Literature

Source	Class	A_V (mag)	SpT	$T_{\rm eff}$ (K)	L_* ($L_\odot$)	$L_{\rm acc}$ ($L_\odot$)	M_* ($M_\odot$)	$\dot{M}_{\rm acc}$ ($M_\odot$ yr^{-1})	References
Gaia21bkw	II	9.8	M4	3190	0.45	$<5\times10^{-3}$[a]	0.25	$<1.5\times10^{-10}$[a]	(1)
Gaia22bvi	flat	2–5	M4	3200	⋯	⋯	0.35	⋯	(2)
Gaia21arv	flat	⋯	K3	4180	⋯	⋯	⋯	⋯	(3, 4)
Gaia23bab	II	5.5[b]–3.2[a]	M1	3630	0.72	3.7[b]	0.4	2×10^{-7}[b]	(5, 6)

Notes.
[a] Value measured in quiescence.
[b] Value measured in burst.
References. (1) E. Fiorellino et al. (2021); (2) S. E. Dahm & L. A. Hillenbrand (2020); (3) M. Kounkel et al. (2019); (4) J. E. Großschedl et al. (2019); (5) T. Giannini et al. (2024); (6) Z. Nagy et al. (2025).

candidates, three objects, namely, Gaia22ehn, Gaia23bri, and Gaia21faq, are present in the catalog of G. Marton et al. (2019), which indicates for them a probability of being a YSO of 80%, 96%, and 86%, respectively. Two of the investigated sources, Gaia22bvi and Gaia23bab, have been previously classified as eruptive variables. Gaia22bvi (i.e., V347 Aur) is an isolated pre-main-sequence star exhibiting periodic brightness variations on timescales of ∼150 days likely related to accretion instabilities (S. E. Dahm & L. A. Hillenbrand 2020). Gaia23bab is a new EXor that has experienced three outbursts of ∼2 mag in roughly 10 yr (2013, 2017, and 2023, T. Giannini et al. 2024; Z. Nagy et al. 2025). The spectrum discussed here was acquired after the most recent outburst in 2023, when the source had returned to a quiescent state. The remaining 14 objects are presented here for the first time. Only two of these objects, Gaia21bkw and Gaia21arv, have been mentioned in two articles not focused on variability studies. In particular, Gaia21bkw is a low-mass source in Perseus and is part of a binary system with a separation of ∼2″ (E. Fiorellino et al. 2021, source #174), while Gaia21arv is included in the APOGEE-2 survey, which examined close companions of YSOs in Orion (M. Kounkel et al. 2019).

Table 2 summarizes the stellar and accretion parameters we compiled from the literature for these four sources (including their evolutionary class, visual extinction, spectral type (SpT), effective temperature, stellar and accretion luminosity, stellar mass, and mass accretion rate). For the subsequent analysis, we will adopt the literature stellar parameters ($T_{\rm eff}$, L_*, M_*) of these sources. The extinction and accretion parameters, which are potentially variable, will be newly estimated using the LBT spectra.

Assuming all our sources are YSOs, we have determined their evolutionary stage using near- and mid-IR photometry from publicly available surveys (Section 2.1) obtained during their quiescent phases. We calculated the spectral index $\alpha = \frac{d\log(\lambda F_\lambda)}{d\log(\lambda)}$ using photometry at 2.16 μm from Two Micron All Sky Survey[19] (2MASS; M. F. Skrutskie et al. 2006) or

[19] https://irsa.ipac.caltech.edu/Missions/2mass.html

LBT Utility Camera in the Infrared[20] (LUCI; W. Seifert et al. 2003) and either 22 μm (AllWISE) or 24 μm (Spitzer-MIPS;[21] G. H. Rieke et al. 2004). Based on the classification scheme by T. P. Greene & C. J. Lada (1996), our sample includes three Class I sources ($\alpha > 0.3$), two flat-spectrum sources ($-0.3 \leqslant \alpha \leqslant 0.3$), and nine Class II sources ($\alpha \leqslant -0.3$). For two sources, Gaia21arv and Gaia21csu, we could not compute α. This was due to the absence of 22/24 μm photometry for Gaia21arv, and because quiescent near-IR photometry is not available for Gaia21csu. The derived values of α for the analyzed sources and the corresponding class are presented in Section 7.3.

2.1. Public Surveys Photometry

To better understand the historical variability of our targets, we have gathered data from several public photometric surveys, including optical data from Gaia, Pan-STARRS, and ZTF, and IR data from NEOWISE.

Pan-STARRS generally offers light curves in the *grizy* filters from 2009 to 2014, with measurements roughly every one to two years. Since 2015, optical light curves have been more frequently sampled in the Gaia *G* filter ($\lambda_{\rm eff} = 6251.50$ Å), typically with 4 to 10 observations per year. The *gri* filters of ZTF have provided better sampling since 2018, with data points ranging from daily to monthly intervals. The NEOWISE survey provides the 3.4 and 4.6 μm magnitudes from mid-2014 until 2024, typically twice per year. Additional photometry is provided by 2MASS in the JHK_s bands, and, for some of our sources, by Akari[22] (H. Murakami et al. 2007) at 9, 18, 65, 90, 140, and 160 μm, by AllWISE at 3.4, 4.6, 12, and 22 μm, and by Spitzer at 3.6, 4.5, 5.8, 8.0, and 24 μm.

2.2. Distances

As shown in Table 1, distance estimates are available in the literature for Gaia21bkw, Gaia22bvi, Gaia22ehn, Gaia23bab, and Gaia21fji. For the other sources, we determined the distance using the following method. The distance of each source was estimated by considering the distance of the nearby clusters taken from E. L. Hunt & S. Reffert (2024). In columns 1–3 of Figures 1 and 2, we show: (1) the spatial distribution of the cluster members and targets, including proper motions represented as arrows; (2) the distance distributions alongside the photogeometric distances of the targets, with their uncertainties, and (3) the proper motion distributions. To further validate distances and potential cluster membership, we additionally examined the extinction distribution toward the targets (Figures 1 and 2, column 4), using 3D dust maps from the Python package *dustmaps* (G. M. Green 2018). For YSOs with distances less than 1.2 kpc, we used the dust map of G. Edenhofer et al. (2024); for more distant YSOs, we used the dust map *Bayestar19* of G. M. Green et al. (2019). We also estimated and validated the distance by identifying the location where the derivative of the extinction versus distance relation is largest. If multiple extinction rises are visible, we adopted the value closest to the cluster distance. In Appendix A, we provide a detailed discussion of the distance determination for each source.

[20] https://scienceops.lbto.org/luci/
[21] https://www.spitzer.caltech.edu/
[22] https://www.ir.isas.jaxa.jp/AKARI/Archive/

3. Observations and Data Reduction

Our observations were conducted between 2021 October and 2024 June as part of a filler program at the 8.4 m LBT, located at Mount Graham, Arizona, USA. We acquired optical and near-IR spectra of our targets using the Multi-Object Double Spectrograph (MODS;[23] R. W. Pogge et al. 2010) and the LBT-LUCI (W. Seifert et al. 2003), respectively.

The journal of observations is given in Table 3. We successfully obtained simultaneous optical and near-IR spectra for Gaia21aul and Gaia21faq. Unfortunately, simultaneous observations for the other targets were not possible due to technical issues or unfavorable weather conditions. Spectra for Gaia22dbd, Gaia21ebu, Gaia23bab, and Gaia23dhi were obtained on subsequent or close nights. For Gaia21bkw, Gaia22efa, Gaia22bvi, Gaia23bri, and Gaia21csu, there is a separation of one to some months between the optical and near-IR spectra. For the remaining targets (Gaia22ehn, Gaia21arv, Gaia24afw, Gaia24beh, and Gaia21fji), we have only obtained either the optical or the near-IR spectrum. Additionally, we acquired an extra near-IR spectrum for both Gaia21bkw and Gaia23bri.

The MODS observations were conducted using the dual grating mode, which covers a spectral range of 350 to 950 nm across the blue and red channels. We used a 0.″80 slit, resulting in a spectral resolution of $\mathfrak{R} \sim 1500$ in the blue channel and $\mathfrak{R} \sim 1800$ in the red channel. To minimize any wavelength-dependent effects on the slit transmission, the slit angle was aligned with the parallactic angle. The specific observation dates and the corresponding integration times can be found in Table 3.

LUCI observations were carried out with the G200 low-resolution grating coupled with the 0.″75 slit. Two datasets were acquired with the standard ABB′A′ nodding technique using the *zJ* and *HK* grisms. This resulted in a final spectrum spanning the 1.0−2.4 μm wavelength range, with a spectral resolution of $\mathfrak{R} \sim 1500$. The integration time for each individual source can be found in Table 3.

The data reduction process was carried out using the Spectroscopic Interactive Pipeline and Graphical Interface (A. Gargiulo et al. 2022), which is specifically developed for reducing long-slit MODS and LUCI spectra.

For each MODS spectral image, the data reduction involved several steps: dark and bias correction, bad-pixel mapping, flat-fielding, and the extraction of the one-dimensional spectrum by integrating along the stellar trace in the spatial direction. Wavelength calibration was achieved using arc lamp spectra.

To ensure accurate alignment between the blue and red spectral segments, we verified the intercalibration by superimposing the spectral range of 5300–5900 Å, which is common to both channels. Our analysis indicated that the blue and red spectra were optimally aligned in all cases, without requiring any further corrections.

The raw LUCI spectral images were cleaned for bad pixels, flat-fielded, sky-subtracted, and corrected for optical distortions in both the spatial and spectral directions. Telluric absorption features were subsequently removed using the normalized spectrum of a telluric standard star, from which its hydrogen recombination lines were also removed. Finally, wavelength calibration was performed using arc lamp spectra.

[23] https://scienceops.lbto.org/mods/

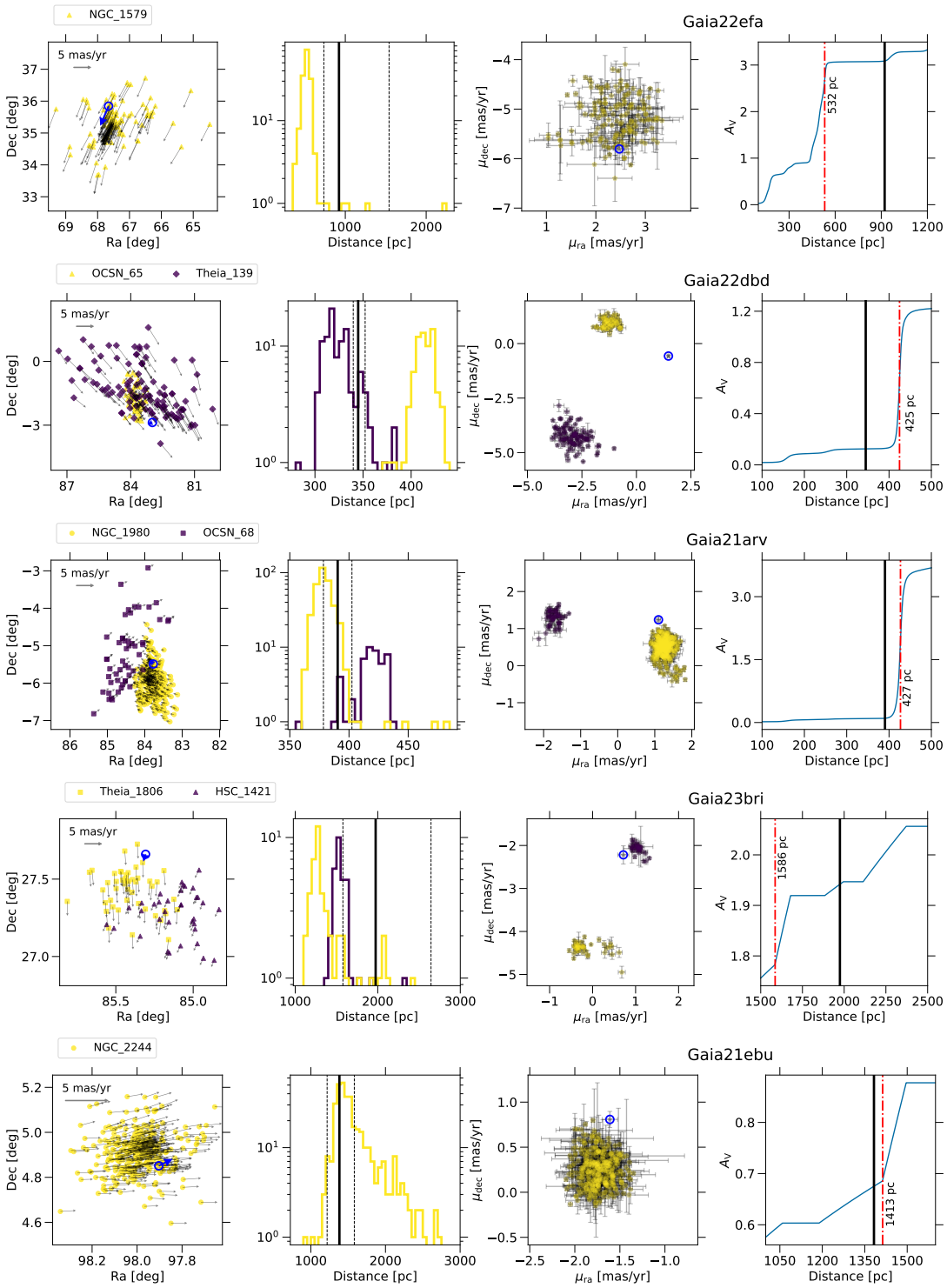

Figure 1. Columns 1–3: clusters from E. L. Hunt & S. Reffert (2024) close to the target YSOs. Different clusters are depicted with different colors and symbols, as indicated on top. Column 1: Spatial distribution of cluster members. The target YSO is shown as a blue circle. Arrows indicate proper motions. Column 2: histogram of the distance distribution. The solid and dashed vertical line represents the distance and its uncertainties of the target YSO from C. A. L. Bailer-Jones et al. (2021). Column 3: proper motion distribution with uncertainties. The target YSO is shown as a blue circle. Column 4: extinction distribution along the line of sight toward the target. The solid vertical line shows the photogeometric distance from C. A. L. Bailer-Jones et al. (2021). Dashed vertical lines mark the distance of the largest extinction increase. See Section 2.2 for details.

Flux losses within the slits were accounted for by utilizing photometry from acquisition images in the *grzi* and *JHK*$_s$ bands, each obtained from the combination of five dithered frames. The photometric points of the target were obtained by using as references all the visible stars in the $6' \times 6'$ ($4' \times 4'$) MODS (LUCI) field. For these reference stars, we accessed

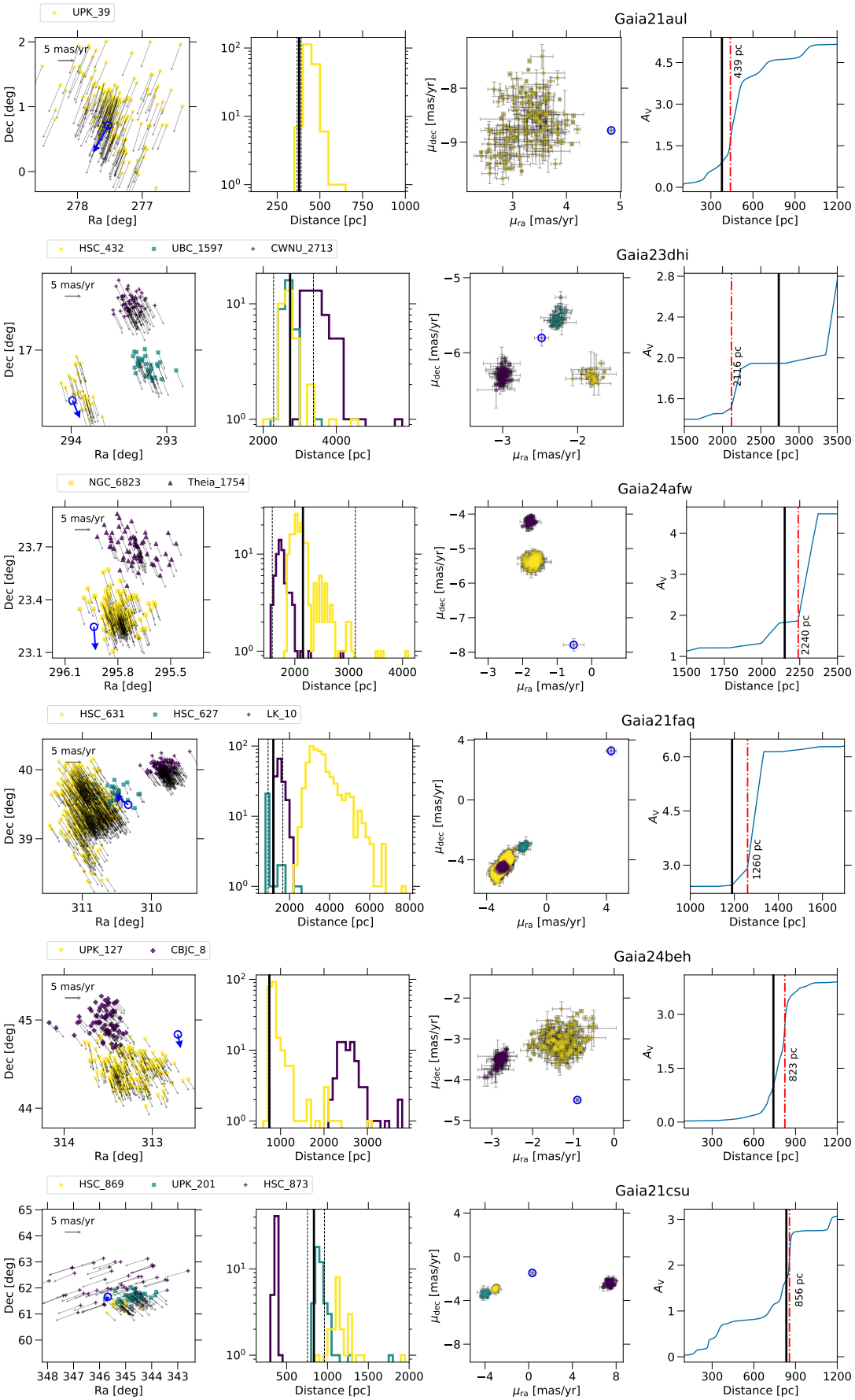

Figure 2. Continuation of Figure 1.

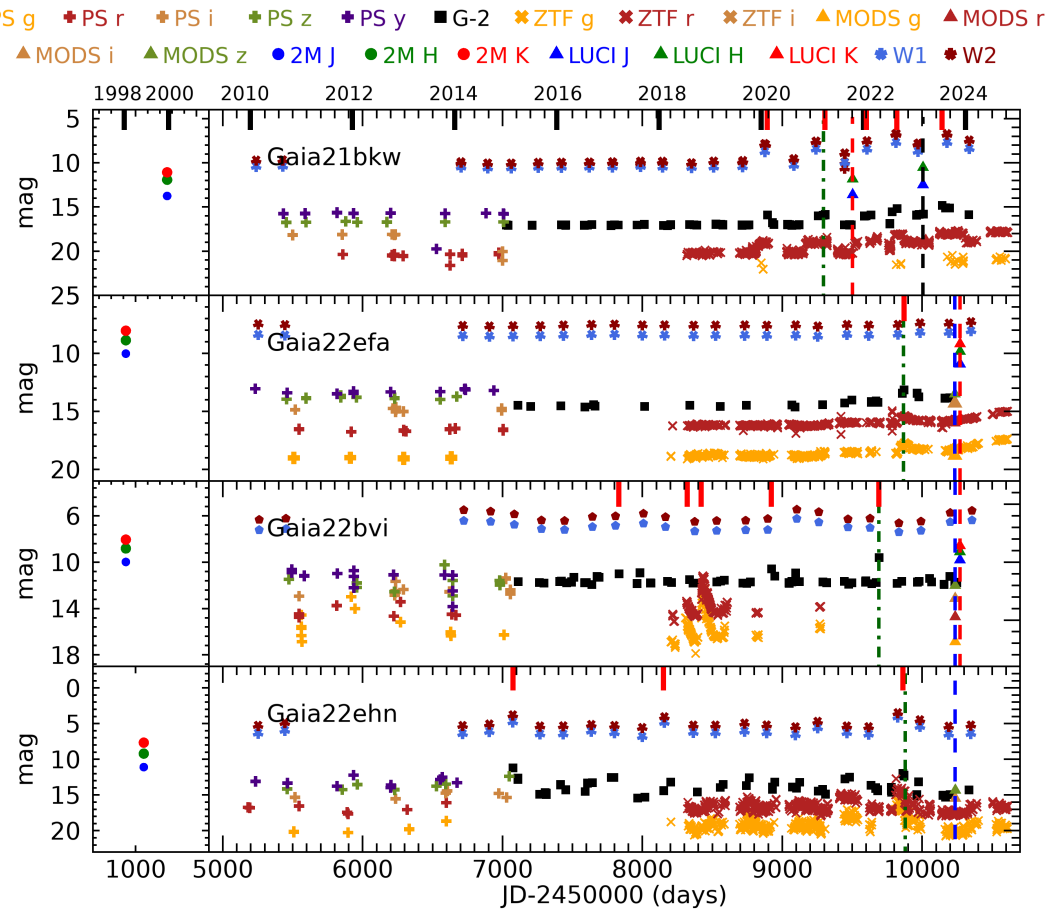

Figure 3. Light curves of Gaia21bkw, Gaia22efa, Gaia22bvi, and Gaia22ehn. Symbols and colors identify data points from different surveys as reported in the legend. Black ticks indicate the date of January 1 of the year displayed on top. Vertical dashed lines mark the dates of the LBT observations (blue: MODS, red: LUCI, black: MODS/LUCI spectra taken on close dates). The green dotted–dashed line marks the date of the Gaia alert. The red ticks on top indicate the dates of optical bursts (see also Table 7).

Table 3
Journal of Observations

ID	Source	MODS			LUCI		
		Date	MJD	T_{int} (B/R) (s)	Date	MJD	T_{int} (zJ/HK) (s)
1	Gaia21bkw	2023 Mar 5	60008	—/1800	2021 Oct 15	59502.3	3600/2700
		…	…	…	2023 Feb 28	60003.1	600/600
2	Gaia22efa	2023 Oct 17	60234.4	1800/1800	2023 Nov 23	60271.4	450/375
3	Gaia22bvi	2023 Oct 19	60236.3	1800/1800	2023 Nov 22	60270.5	750/1200
4	Gaia22ehn	2023 Oct 21	60238.3	1800/4500	…	…	…
5	Gaia22dbd	2024 Jan 10	60319.3	1800/1800	2024 Jan 9	60318.2	1800/1800
6	Gaia21arv	…	…	…	2021 Oct 15	59502.4	1800/1800
7	Gaia23bri	2023 Oct 19	60236.4	900/1800	2023 Nov 23	60271.4	2925/—
		…	…	…	2024 Jan 9	60318.4	4050/3600
8	Gaia21ebu	2024 Jan 10	60319.4	1800/1800	2024 Jan 9	60318.3	1800/1800
9	Gaia21aul	2023 Jun 4	60099.3	600/600	2023 Jun 4	60099.2	1780/160
10	Gaia23bab	2024 Apr 11	60411.5	1800/4050	2024 Apr 14	60414.4	1800/1800
11	Gaia23dhi	2024 Jun 7	60468.4	1800/900	2024 Jun 10	60471.4	900/900
12	Gaia24afw	2024 Jun 7	60468.5	900/1800	…	…	…
13	Gaia21faq	2023 Jun 4	60099.4	1350/—	2023 Jun 4	60099.3	550/1800
14	Gaia24beh	2024 Jun 8	60469.4	1800/1800	…	…	…
15	Gaia21fji	2023 Oct 19	60236.2	1800/1800	…	…	…
16	Gaia21csu[a]	2023 Oct 19	60236.3	1350/1800	2024 Jan 9	60318.1	3600/3600

Note.
[a] For this source, we obtained additional photometry on 2022 December 17 (MJD = 59930).

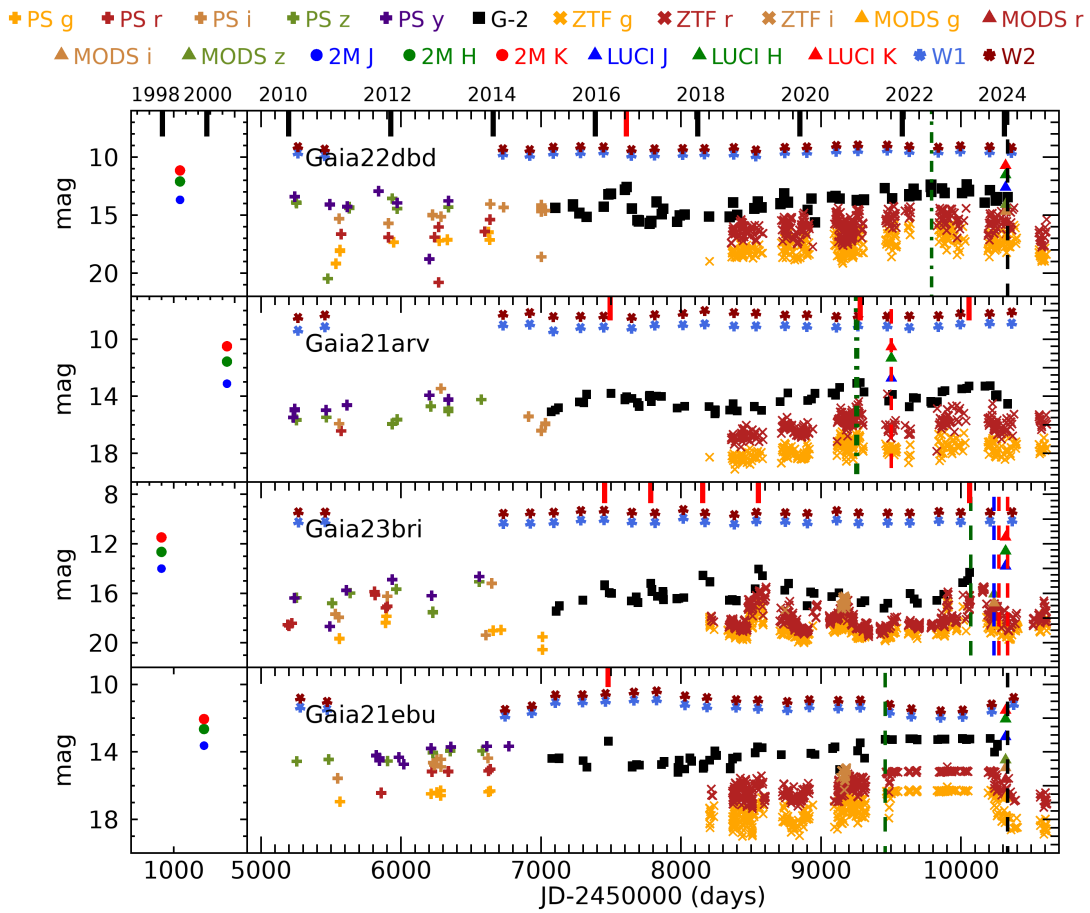

Figure 4. Light curves of Gaia22dbd, Gaia21arv, Gaia23bri, and Gaia21ebu. Symbols and colors are the same as in Figure 3.

publicly available optical/near-IR photometry from either the Pan-STARRS catalog or the 2MASS catalog. The resulting magnitudes are given in Appendix B.

Given that the optical and near-IR spectra for most sources were obtained several months apart, we chose not to realign the MODS and LUCI spectra. This decision was made because a variability of a few tenths of a magnitude could have occurred between the two observation dates. For the two sources with nearly simultaneous MODS and LUCI observations, the alignment between the optical and near-IR spectra was within a few percent, and no additional adjustments were necessary.

4. Description of the light Curves

The assembled light curves for the targets are presented in Figures 3–6. These figures include photometric data gathered from public surveys (as detailed in Section 2.1) along with the LBT photometry provided in Appendix B. The NEOWISE light curves show a photometric point every six months, obtained by averaging the single-epoch photometry taken in each season. The single-epoch data points have been checked for saturation and, if needed, corrected following the saturation corrections of R. M. Cutri et al. (2015). The AllWISE photometric data obtained in 2010 at 3.4 and 4.6 μm have also been shown for completeness. In the forthcoming Section 8.1, we will discuss these light curves from a general point of view, while here we present the light curves of the individual sources.

1. *Gaia21bkw* was alerted by Gaia on 2021 March 19, due to a rapid brightening of 1 mag in the *G* band. It is worth noting that a prior burst event occurred in 2020, but no alert was issued at that time. Following this initial alert, the source exhibited three additional burst episodes in 2022 January, 2022 August, and 2023 March. The most recent event was the most significant, reaching a peak magnitude of 2.2 above the quiescent level of ∼19 mag in the *G* band. All observed outbursts have had durations ranging from about six months to a year and have also been observed by NEOWISE, with amplitudes similar to those in the optical. The first LUCI spectrum was taken during a period of quiescence, while subsequent MODS/LUCI spectra were obtained during a rising phase of the last outburst, although not at its peak.
2. *Gaia22efa*. The Gaia alert was issued on 2022 August 6, following a brightening event of approximately one magnitude. After this episode, the source returned to a quiescent state before beginning to increase in brightness again in 2024. This new rise, which started after the conclusion of the Gaia mission, has been observed by ZTF in the *g* and *r* bands. Our observations cover the initial part of this renewed brightening phase.
3. *Gaia22bvi*. The Gaia alert was released on 2022 April 22. However, the source had exhibited earlier brightness variations of smaller amplitudes, which were also detected by NEOWISE and ZTF. This latter, in particular, recorded two additional bursts in 2018 that

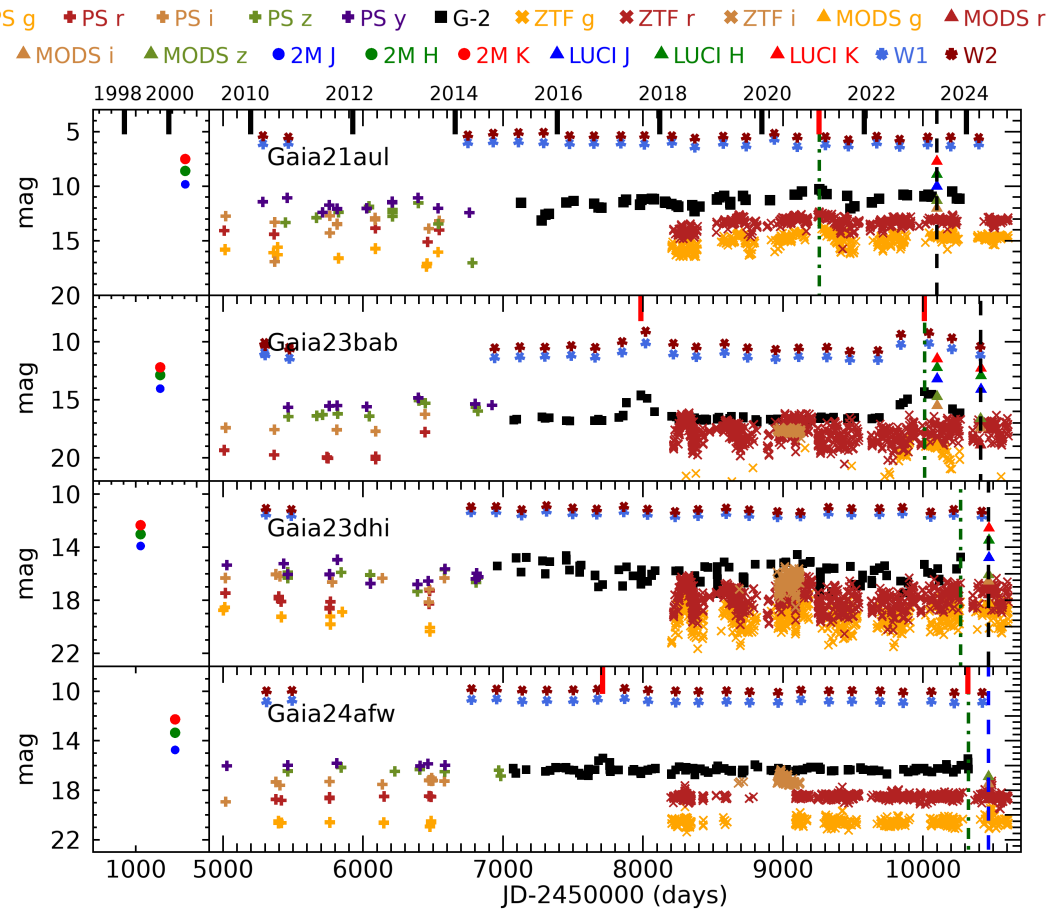

Figure 5. Light curves of Gaia21aul, Gaia23bab, Gaia23dhi, and Gaia24afw. Symbols and colors are the same as in Figure 3.

were not sampled by Gaia. Our observations were conducted while the source was in a quiescent state.

4. *Gaia22ehn*. This source displays significant variability, with peak-to-peak amplitudes reaching up to 4 mag in the *G* band and 2 mag in the NEOWISE bands. The alert was issued on 2022 October 10, but our observations, conducted approximately a year later, did not capture this peak as the source had returned to a quiescent state by then. Two further outbursts have occurred: the first in early 2015 at the beginning of the Gaia mission, and a second in early 2018, particularly bright in the NEOWISE bands.
5. *Gaia22dbd*. The source exhibited a significant brightening event in 2016 that lasted for about a year, which was not alerted by Gaia. After a period of roughly one year of reduced activity, the brightness steadily rose again, peaking in 2023, when the alert was issued. Our observations cover the initial part of a declining phase in 2024 January.
6. *Gaia21arv*. Gaia alerted this source on 2021 February 9. Two other peaks were observed in 2016 April and 2023 August. The NEOWISE light curve shows a magnitude modulation of several tenths of magnitude in both the 3.4 and 4.6 μm filters, which is also noticeable in the Gaia and ZTF light curves. It appears to consist of a longer timescale variability component, with an amplitude of approximately 2 mag and a duration of about 3 yr, upon which a faster variability with a period of roughly 200 days and an amplitude of about 1 mag is superimposed. Our observations have been obtained during the fading phase after the 2021 burst.
7. *Gaia23bri*. The alert was issued on 2023 April 27, but similar brightening events occurred between 2016 and 2019. The light curve shows stochastic variations, which are also visible in the NEOWISE light curve, though with a lower amplitude. We observed Gaia23bri with MODS around its last peak brightness and continued to monitor its decline over the following months using LUCI.
8. *Gaia21ebu*. The Gaia light curve indicates an initial peak around 2016 April, though the monitoring around this event was somewhat limited. Subsequently, in late 2018, the brightness began a gradual increase of approximately 1.7 mag over three years. This rise culminated in a plateau phase, which triggered the alert. This plateau lasted for about two years, from 2021 to 2023, until the end of the Gaia monitoring. Subsequently, ZTF observed a sharp decline in brightness. Our LBT spectra were obtained at the onset of this new declining phase. Interestingly, the NEOWISE light curve exhibits a different behavior compared to the optical variations. Instead, it shows gradual fluctuations with an amplitude of about 2 mag on timescales of roughly 1000 days, contrasting with the observed optical changes.
9. *Gaia21aul*. This source presents lower amplitude variability. Noticeably, *g*- and *r*-band photometries

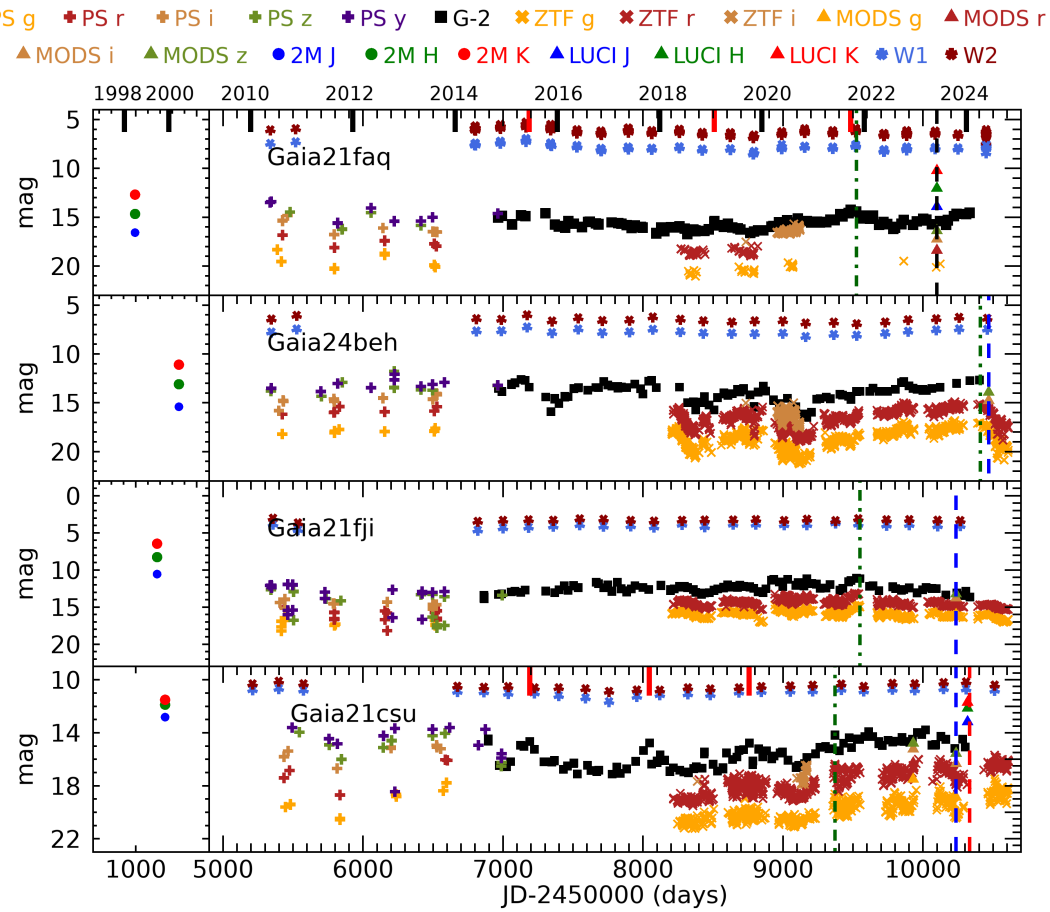

Figure 6. Light curves of Gaia21faq, Gaia24beh, Gaia21fji, and Gaia21csu. Symbols and colors are the same as in Figure 3.

recorded by Pan-STARRS during the 2009–2014 period appear to be at a lower brightness level compared to those measured by ZTF after 2017. The Gaia alert, issued on 2021 February 13, coincided with the peak of a gradual and sustained increase in brightness. Our observations were conducted during a period of lower brightness. The NEOWISE light curve exhibits irregular variability that does not follow the same pattern as the optical light curve.

10. *Gaia23bab*. The light curve has been commented on in detail by T. Giannini et al. (2024) and Z. Nagy et al. (2025). Here, we only remark that the new LBT spectra have been taken in the quiescent phase after the 2023 outburst.
11. *Gaia23dhi*. This source exhibits irregular variability in both amplitude and timescale. The alert, issued on 2023 November 21, does not show a definite peak in brightness. Our observations were conducted when the source was at an intermediate level of brightness.
12. *Gaia24afw*. The light curve for this source appears to be relatively stable, showing a typical modulation of around 0.5 mag. Notably, two bright peaks, each with an amplitude of approximately 1 mag and lasting about a month, were recorded in 2016 November and 2024 January. The alert for this source was triggered following the latter peak, and our observations were conducted immediately after this event.
13. *Gaia21faq*. This object exhibited an erratic brightening of approximately 2 mag, a variability that is also clearly evident in the NEOWISE bands. The Gaia light curve shows three distinct peaks occurring around 2015 August, 2019 January, and 2021 September, when the alert was issued. Subsequently, the source underwent a short period of fading before its brightness started to increase again, at which point we obtained our LBT spectra.
14. *Gaia24beh*. Between 2014 and 2021, this source underwent erratic variability with a peak-to-peak amplitude reaching up to 3 mag. Following this period, the brightness began to increase, culminating in a peak on 2024 April 2, which triggered the Gaia alert. Our observations roughly coincide with this peak. Furthermore, new ZTF photometry suggests that a sudden decline in brightness is currently underway.
15. *Gaia21fji*. This source exhibits a continuous brightness modulation with a peak-to-peak amplitude exceeding 2 mag. This variability is also noticeable in the NEOWISE light curve, although with a smaller amplitude. The MODS spectrum was obtained when the source was close to its minimum brightness.
16. *Gaia21csu*. Also, this source presents significant brightness variations, with peak-to-peak changes of more than 3 mag in *G*. Peaks were registered in 2015 June, 2017 October, and 2019 October. Following the last peak, the source started a continuous brightening trend, which triggered an alert on 2021 June 6. Since 2022, the light curve has reached a plateau phase, during which we acquired our LBT spectra.

Table 4
Extinction Determinations

ID	Source	Quiescence			Intermediate			Outburst		
		Cont.	Lines	Col–Col	Cont.	Lines	Col–Col	Cont.	Lines	Col–Col
1	Gaia21bkw	⋯	10.0	9.8	10.0	10.0	10	⋯	⋯	⋯
2	Gaia22efa	5.0	6.1	2	⋯	⋯	⋯	⋯	⋯	2
3	Gaia22bvi	3.2	2.8	3	⋯	⋯	⋯	⋯	⋯	⋯
4	Gaia22ehn	6.0	5.0	5	⋯	⋯	⋯	⋯	⋯	⋯
5	Gaia22dbd	⋯	⋯	7	2.2	⋯	⋯	⋯	⋯	1
6	Gaia21arv	⋯	⋯	6	6.6[a]	⋯	6	⋯	⋯	⋯
7	Gaia23bri	2.4	2.3	⋯	⋯	⋯	2.5	⋯	⋯	⋯
8	Gaia21ebu	⋯	⋯	3	2.0	⋯	3.5	⋯	⋯	⋯
9	Gaia21aul	4.0	4.0	$\gtrsim$3	⋯	⋯	⋯	⋯	⋯	⋯
10	Gaia23bab	3.2	4.3	3.5	⋯	⋯	⋯	5.5 (1)	⋯	⋯
11	Gaia23dhi	⋯	⋯	⋯	2.0	⋯	3	⋯	⋯	0
12	Gaia24afw	4.0	5.0	4	⋯	⋯	⋯	⋯	⋯	⋯
13	Gaia21faq	⋯	⋯	5	6.0	5.0	5	⋯	⋯	⋯
14	Gaia24beh	⋯	⋯	$\gtrsim$10	⋯	⋯	⋯	5.2	5.2	⋯
15	Gaia21fji	⋯	⋯	10	⋯	⋯	⋯	3.5	4.4	⋯
16	Gaia21csu	3.8	3.0	⋯	1.4	⋯	3	⋯	⋯	2.5

Note.
[a] In this source, we fitted the shape of the near-IR continuum.
Reference. (1) T. Giannini et al. (2024).

5. Extinction

As anticipated in Section 2, the observed variability might be at least partially due to changes in extinction along the line of sight. Therefore, precisely measuring extinction during different brightness phases is essential to distinguish extinction- from accretion-driven variability. In this section, we introduce the three methods used to compute A_V, deferring the detailed description of each method to the subsequent relevant Sections 6.2, 7.1, and 7.4. In particular, we used: (1) the "photometric" method, based on the analysis of the near-IR colors (Section 6.2), (2) the optical "continuum-fitting" method, which relies on the slope of the optical continuum (Section 7.2), and (3) the "line-fitting" method, which considers the A_V value providing consistency among different accretion lines (Section 7.4). The resulting A_V values, presented in Table 4, generally agree within 1 mag. The "continuum-fitting" method provides A_V with a typical uncertainty of 0.2−0.3 mag. The other two methods are less robust. The "line-fitting" method's reliability depends heavily on the number of observed emission lines and on the uncertainty in measured fluxes and adopted empirical relations. The "photometric" method assumes that the observed sources are low-mass T Tauri stars and that the effect of scattering due to any residual circumstellar material is negligible. We estimate the uncertainty on A_V of these two methods to be around 0.5−1 mag. As a general strategy, we will adopt the A_V derived from the "continuum" method whenever possible, and the "line-fitting" and "photometric" methods in the other cases.

6. Photometric Analysis

6.1. SEDs

Figures 7–10 show the SED of our sources, obtained by collecting LBT photometry and public archival data. The details of the SED of each source are commented on in Appendix A, while here we give some general information. The red points represent the quiescence data, which have been taken typically on dates that may differ by several years. In the case of multiple observations in a given band (in particular, Pan-STARRS, ZTF, Gaia, and NEOWISE data), the plotted data points represent the average of the photometric measurements from the light curve that do not exceed the historical standard deviation by more than 0.5 mag. The photometric points during burst phases are depicted in blue, while intermediate states are in green. For most of the sources, the quiescent photometric points extend up to 10–20 μm (AllWISE or Spitzer data), while the burst data typically extend up to $\sim$5 μm (NEOWISE data).

First, it is worth noting that all the sources display an SED characteristic of a YSO. In particular, they show a peak in the near-IR or at even longer wavelengths, along with a significant IR excess. These characteristics strongly support the classification as YSOs of the objects classified by Gaia as "YSO candidates" (see Table 1).

We plot in the same figures the blackbody (BB) function at the effective temperature ($T_{\rm eff}$) of the stellar photosphere (Section 7.2) and reddened using the A_V value measured during quiescence (Table 4). The BB was normalized using the J-band photometry in the quiescent phase, with the assumption that at wavelengths around 1 μm the emission originating from the accretion shock and the disk is minimal compared to the emission from the stellar photosphere.

For Gaia21bkw, Gaia22bvi, Gaia21arv, and Gaia23bab, $T_{\rm eff}$ was taken from the literature (Table 2), while the A_V values in quiescence were estimated based on the near-IR colors in the case of Gaia21bkw and Gaia21arv and from the continuum fitting in the case of Gaia22bvi and Gaia23bab. For the other sources observed in the optical range during quiescence, $T_{\rm eff}$ and A_V were adopted from the continuum-fitting method, as will be discussed in Section 7.2. This applies to Gaia22efa, Gaia22ehn, Gaia23bri, Gaia21aul, Gaia24afw, and Gaia21csu. For Gaia22dbd, Gaia21ebu, and Gaia21fji, which were observed either during a burst or in an intermediate brightness

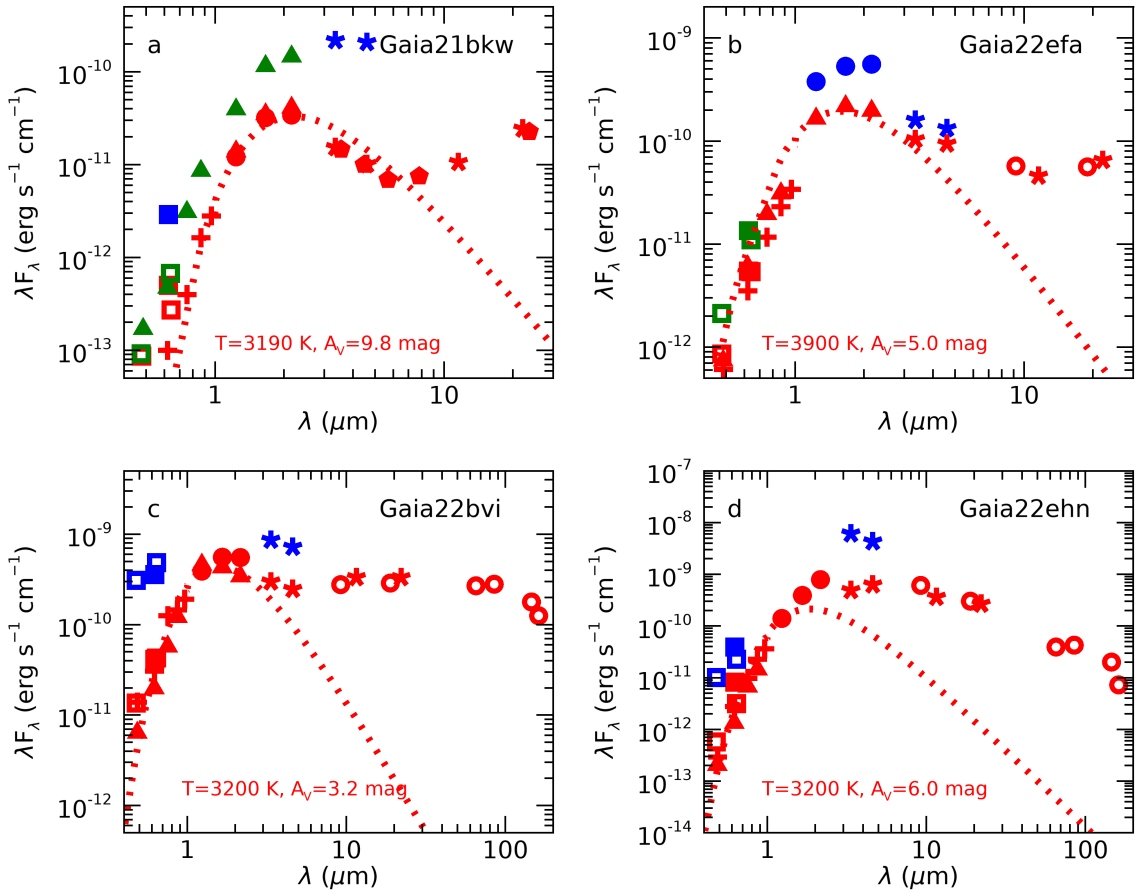

Figure 7. SED of Gaia21bkw (a), Gaia22efa (b), Gaia22bvi (c), and Gaia22ehn (d). Quiescence, intermediate, and burst states are colored in red, green, and blue, respectively. Symbols have the following meaning. Crosses: Pan-STARRS; open squares: ZTF; filled squares: Gaia; filled triangles: LBT; filled circles: 2MASS; asterisks: AllWISE/NEOWISE; filled diamonds: Spitzer; open circles: Akari. The dotted line indicates the reddened BB function representative of the stellar emission. The adopted temperature and extinction are reported as well.

state, we estimated A_V using the near-IR 2MASS colors in quiescence (Section 6.2). In the case of Gaia23dhi, which was observed with 2MASS during a burst, we estimated A_V from the LUCI colors during an intermediate phase of brightening and used the same value also to redden the BB function in quiescence. For these latter four sources, we adopted the $T_{\rm eff}$ values determined as discussed in Section 7.2. Finally, note that for Gaia21faq and Gaia24beh, we were unable to constrain $T_{\rm eff}$ and therefore we did not attempt to plot the BB function (Section 7.2).

The integral under the BB is taken as an estimate of the stellar luminosity (L_*) and compared with that presented in the forthcoming Section 7.3. The two determinations differ in most cases by a few percent, the largest differences being in Gaia22efa, Gaia23bri, Gaia21aul, and Gaia21fji (30%−50%).

6.2. Color–Color Diagrams

The $[g-r]$ versus $[r-i]$ and $[J-H]$ versus $[H-K_s]$ two-color diagrams for the targets are presented in Figure 11. In these diagrams, data points are color coded to represent different states: red for quiescent, green for intermediate, and blue for burst. The arrows in the plots indicate the direction of the extinction vector, following the reddening law of J. A. Cardelli et al. (1989). In the plots, the black segments connect data points of the same source observed in different brightness phases. It is noteworthy that most of these segments are not aligned with the extinction vector, which implies that changes in extinction play a relatively minor role in the observed variability. An A_V estimate was obtained from the near-IR colors by de-reddening the observed data until they overlap with the *locus* of the unreddened T Tauri stars (M. R. Meyer et al. 1997), which is depicted with a dotted line in the right panel of Figure 11. Based on this analysis, we conclude the following: (1) in general, our sources are subject to visual extinction ranging from 0 to 10 mag; (2) these A_V estimates may increase if the source were a Herbig Ae/Be star, whose *locus* is located at lower values of the $[J-H]$ color (J. Hernández et al. 2005). As we will show in Section 7.3, this prescription applies in particular to sources #9 and #15, whose A_V estimate is given as a possible lower limit in Table 4; (3) the colors for sources #13 and, to a lesser extent, #14, extend beyond the region of the observed T Tauri stars. For these sources, the A_V estimated by ideally elongating the T Tauri straight line should be taken with some caution.

With some exceptions, both optical and near-IR colors become bluer during burst phases. The average color differences observed between quiescence and bursts are as follows: $\Delta([g-r]) = 0.27 \pm 0.08$, $\Delta([r-i]) = 0.37 \pm 0.12$,

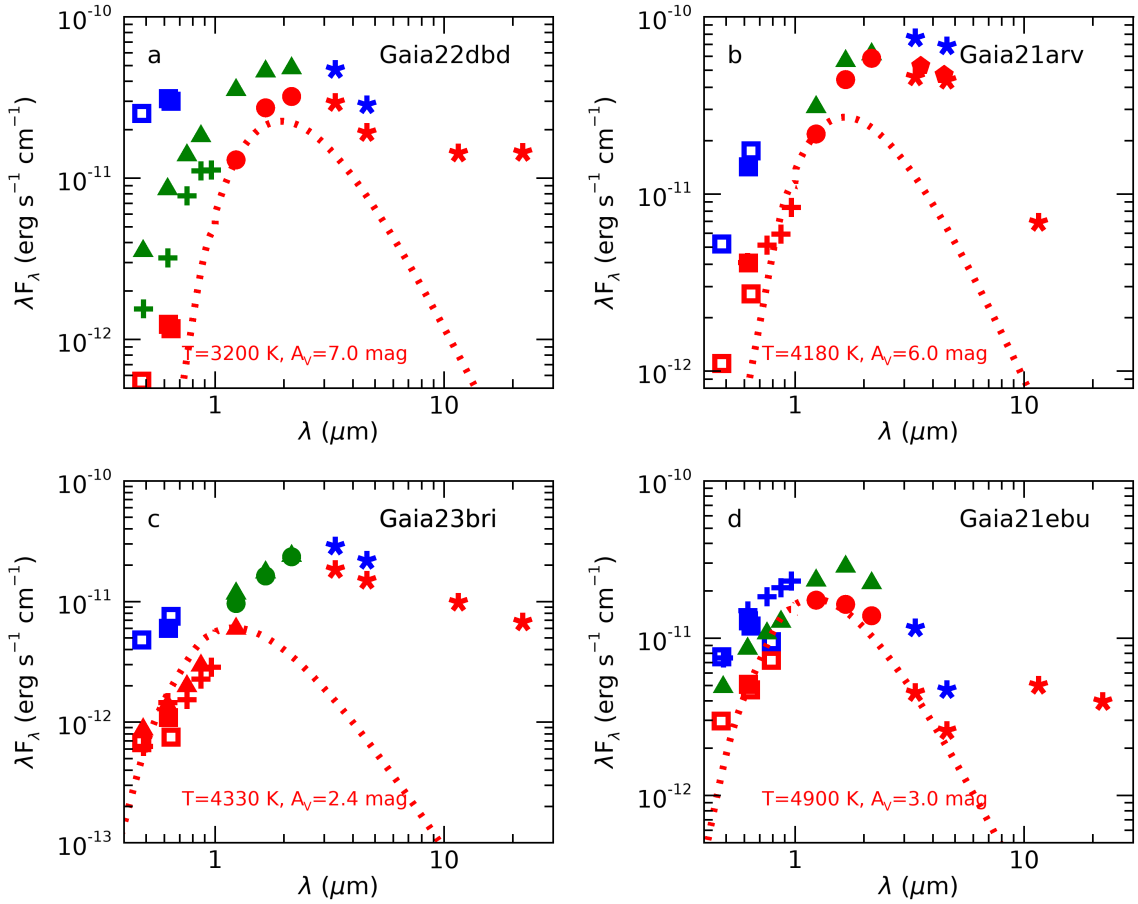

Figure 8. As in Figure 7 for Gaia22dbd (a), Gaia21arv (b), Gaia23bri (c), and Gaia21ebu (d).

$\Delta([J-H]) = 0.58 \pm 0.23$, and $\Delta([H-K_s]) = 0.50 \pm 0.21$. We interpret this blueing as evidence that the observed bursts are episodes of enhanced accretion. Indeed, this effect is commonly attributed to both the clearing of dust during the burst events (e.g., L. A. Hillenbrand et al. 2019) and the increasing contribution of accretion luminosity at UV wavelengths (e.g., L. Venuti et al. 2014). This interpretation is further supported by the smaller variation observed in the NEOWISE colors, $\Delta([W1 - W2]) = 0.05 \pm 0.02$, indicating that typically the outer regions of the disks are less affected by the burst heating.

7. Spectroscopic Analysis

7.1. Description of the Spectra

We show in Figure 12 the spectrum of Gaia23bab, as an example of the observed spectra. This is the only object in our sample for which we have spectra from both its burst phase (as reported in T. Giannini et al. 2024) and its quiescent state. The MODS and LUCI spectra for all the remaining sources in our study can be found in Appendix B, Figures 18–32.

All the observed sources share two important characteristics that are typical of accreting YSO spectra: a rising continuum from the optical to the IR wavelengths and the presence of permitted lines in emission. In particular, Hα is observed in emission in all targets, being partially absorbed in Gaia21ebu and Gaia23dhi. The strongest H I lines are seen in burst spectra of Gaia24beh and Gaia21fji (both Class I sources), as well as Gaia23bab, as previously discussed in T. Giannini et al. (2024). Additionally, Ca II, O I, or He I optical lines are detected in all spectra with the exception of Gaia22dbd, Gaia21ebu, Gaia24afw, and Gaia21csu.

More than half of the analyzed spectra exhibit signatures of outflowing gas. The [O I] 6300Å line is detected in the spectra of 10 objects (Gaia22bvi, Gaia22ehn, Gaia23bri, Gaia21aul, Gaia23bab, Gaia24afw, Gaia21faq, Gaia24beh, Gaia21fji, and Gaia21csu), and the [S II] doublet at $\lambda\lambda$ 6717, 6732 Å in five objects (Gaia22ehn, Gaia21fji, Gaia21faq, Gaia24beh, and Gaia21csu). In addition, the [O II] doublet at $\lambda\lambda$ 7320, 7330 Å and the [N II] 6584 Å are detected in the spectrum of Gaia22ehn, while the [N I] 1.04 μm, and [Fe II] 1.25 μm lines are detected in the spectrum of Gaia21faq.

The He I at 1.08 μm is observed in emission or absorption in all LUCI spectra, with the exceptions of Gaia22dbd, Gaia21faq, and Gaia21csu. Additionally, we observe weak H_2 2.12 μm emission in Gaia21arv, Gaia23bab (during its burst phase), and Gaia21faq. Finally, the CO 2–0 or 3–1 bandheads and Na I doublet at 2.2 μm are observed in absorption in Gaia21bkw, Gaia21arv, and in Gaia21csu, in emission in Gaia21faq, and within the burst spectrum of Gaia23bab.

Line fluxes and their corresponding 1σ uncertainties were calculated using the SPLOT task within IRAF. This method considers both the effective readout noise per pixel and the photon noise present in the spectral region encompassing the emission line. The fluxes of the main lines can be found in Appendix C.

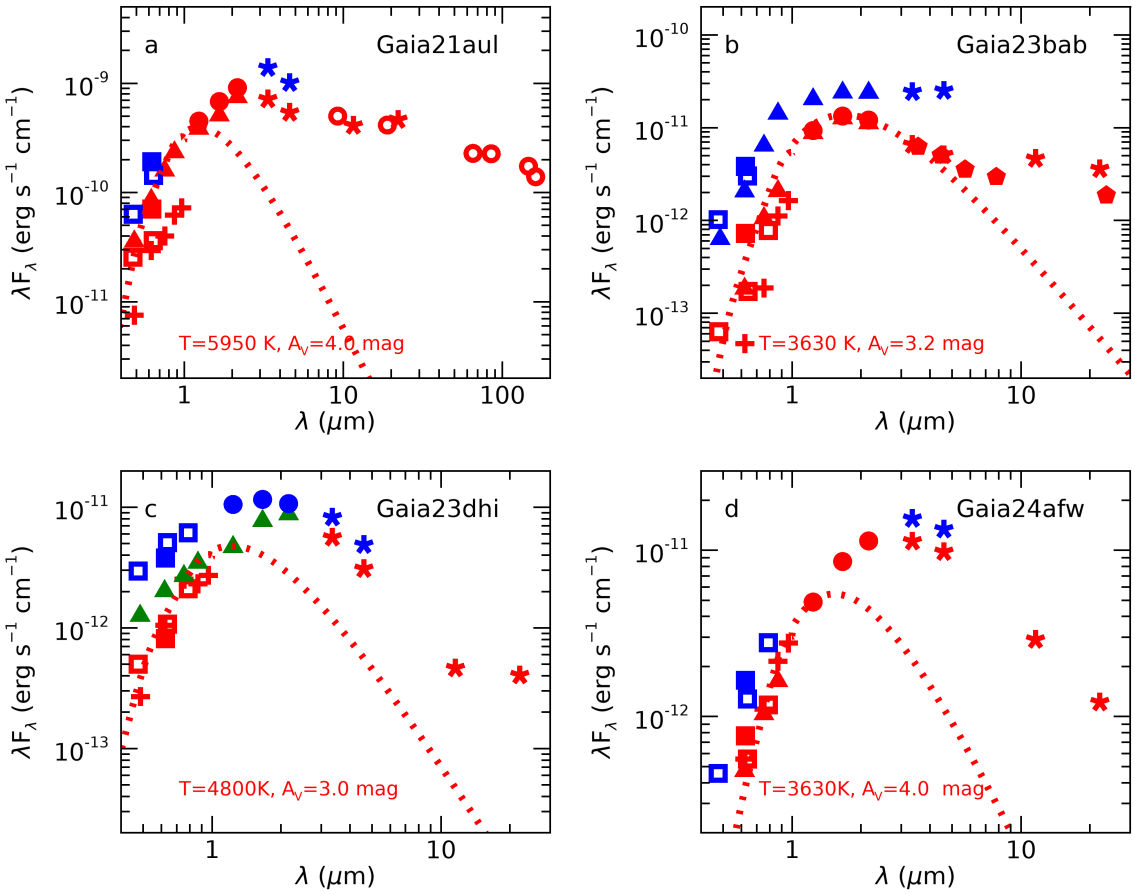

Figure 9. As in Figure 7 for Gaia21aul (a), Gaia23bab (b), Gaia23dhi (c), and Gaia24afw (d).

7.2. Determination of the Spectral Type

The first step of our study involves determining the stellar parameters of our sample sources, beginning with their SpT. As detailed in Section 2 and Table 2, this is currently known for only four sources: Gaia21bkw, Gaia22bvi, Gaia21arv, and Gaia23bab.

The standard approach for estimating SpT typically involves comparing optical photospheric lines with stellar templates. Simultaneously, extinction can be determined from the slope of the continuum. However, in cases of burst accretion, this method becomes complicated due to the presence of excess continuum emission in the UV and IR wavelengths. The UV excess is thought to originate from hot spots formed by the accretion shock on the surface of the star, while the IR excess is generated within the accretion disk itself. During periods of significant burst accretion, the UV–optical excess can become so prominent that in late-type stars, the molecular bands visible in the quiescent spectrum may no longer be detectable. Consequently, a burst spectrum might be misclassified as belonging to an earlier SpT with respect to the star's actual quiescent classification. Examples include ASSASSN-13db, where the ratio $r = \mathrm{Flux(excess)/Flux(star)}$ (veiling) increases from 0.4 in quiescence to over 3 during a burst (T. Giannini et al. 2022), and Gaia23bab, where T. Giannini et al. (2024) incorrectly inferred an SpT earlier than K due to the absence of optical molecular bands in the burst spectrum. For this reason, in the present work, we have focused our continuum-fitting analysis only on quiescence spectra (Gaia22efa , Gaia22ehn , Gaia23bri, Gaia21aul, Gaia24afw, and Gaia21csu) and on spectra of other brightness phases that present prominent absorption features. These are the burst spectrum of Gaia21fji, and the intermediate state spectra of Gaia21ebu and Gaia23dhi, as they show H I lines or the Na I doublet at $\lambda\lambda$5891, 5897 in absorption, which are indicators of an early SpT. Our fitting procedure considers SpT, A_V, and r as variables. The results of this fitting procedure are illustrated in Figures 13 and 14. For late-type spectra, we fitted the continuum portion within the 7000–7200 Å range, which encompasses prominent TiO absorption bands. For early-type spectra, we fitted either the 3700−4500 Å range, where several Balmer lines are located (in Gaia21aul and Gaia21fji), or the spectral region around the Na I doublet at 5890 Å (in Gaia21ebu and Gaia23dhi), following the method of A. Tripicchio et al. (1997) and K. Biazzo et al. (2025, in preparation).

As a strategy, we have first selected a number of BTSettl templates with temperature between 3000 and 7000 K (SpT F−M) and $\log g = 4.5$. An A_V between 0 and 20 mag (in steps of 0.2 mag) and a veiling between 0 and 5 (in steps of 0.1) are then applied to each template to find the values that best match the spectral features and the slope of the continuum observed in our stars. Typically, we derive SpT K−M, A_V between 2 and 6 mag and $r \lesssim 3.0$, with the exception of Gaia21aul and Gaia21fji, for which SpT is G1 and G0, respectively.

A particular case is that of Gaia22dbd. The source was seen during an intermediate state, and the spectrum does not present

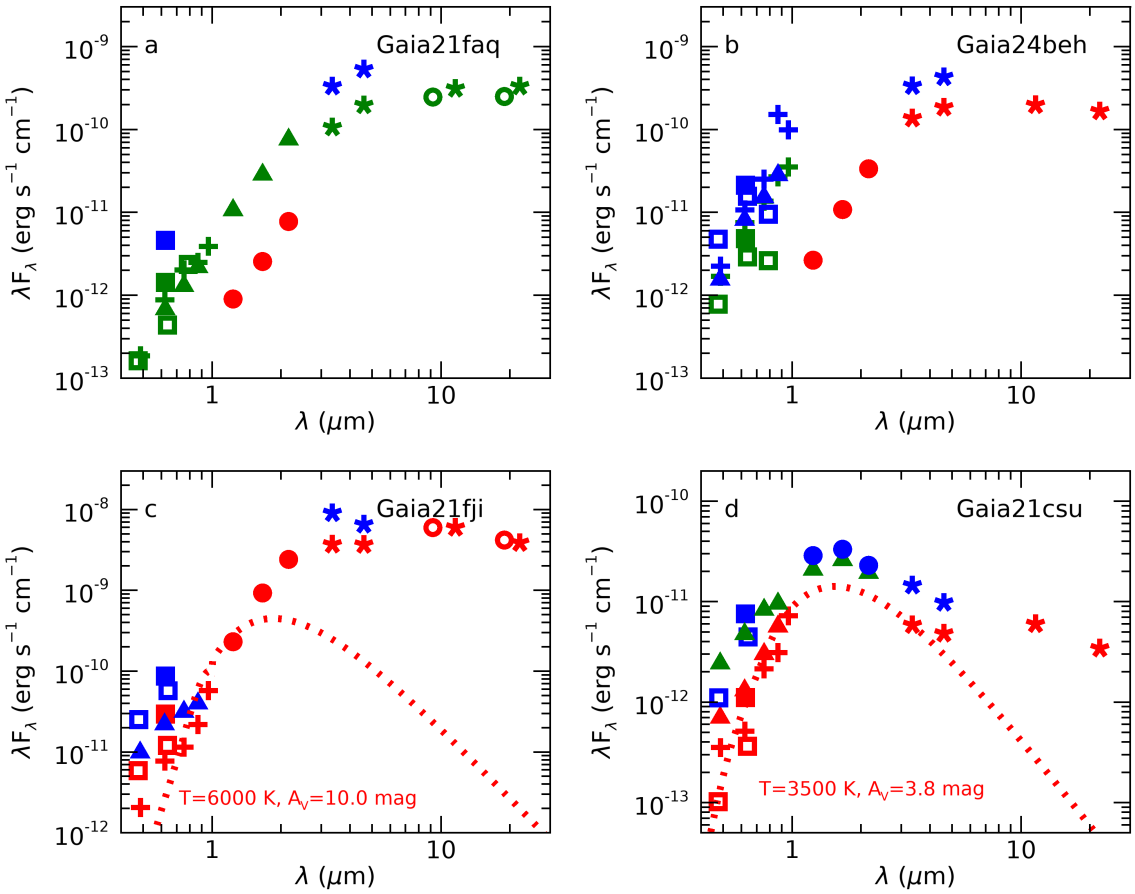

Figure 10. As in Figure 7 for Gaia21faq (a), Gaia24beh (b), Gaia21fji (c), and Gaia21csu (d).

lines or bands in absorption. We have provisionally estimated the effective temperature by fitting the SED through the optical and J photometry in quiescence and assuming the A_V derived from the near-IR colors. Then, this is converted to SpT using the value tabulated in Table 6 of M. J. Pecaut & E. E. Mamajek (2013) for 5 −30 Myr old stars. The estimated uncertainty is about two subclasses. Finally, for Gaia21faq and Gaia24beh, we were unable to derive the SpT because their intermediate and burst spectra do not present absorption features, and there are no optical points available during quiescence to fit the SED with a BB function.

7.3. Other Stellar Parameters

Based on the SpT of our sources, we derived other stellar parameters, including stellar luminosity, radius, and mass. These are reported in Table 5 together with the spectral index α. This derivation was performed using near-IR photometry and considering extinction during the quiescent phase. Assuming that the J-band emission is minimally affected by accretion spots and emission of the circumstellar disk, we calculated the bolometric magnitude ($M_{\rm bol}$) using the formula:

$$M_{\rm bol} = m(J) + 5 - 5\log_{10}[d\,({\rm pc})] + {\rm BC}_J, \quad (1)$$

where $m(J)$ is the extinction-corrected J magnitude, d(pc) is the distance in parsecs, and BC$_J$ is the bolometric correction in the J band. For BC$_J$, we adopted the values provided in Table 6 of M. J. Pecaut & E. E. Mamajek (2013) for sources aged between 5 and 30 Myr. For our objects, which have SpTs ranging from G0 to M4, the corresponding BC$_J$ values are between 0.98 and 1.91. For Gaia21faq and Gaia24beh, we were only able to determine a lower limit for $M_{\rm bol}$. This is because we could not add a BC$_J$ correction in applying Equation (1), as their SpTs are unknown. An estimate of the stellar luminosity, L_*, can be calculated as:

$$\log_{10} L_* = 0.4[M_{\rm bol} - M_{\odot}], \quad (2)$$

where $M_{\odot}$ represents the bolometric luminosity of the Sun, which is equal to 4.74 mag (E. E. Mamajek et al. 2015).

Assuming BB emission, the stellar radius (R_*) can be calculated using the formula:

$$R_* = 1/2\, T_{\rm eff}^2/\sqrt{L_*/\pi\sigma}, \quad (3)$$

where σ is the Stefan–Boltzmann constant and $T_{\rm eff}$ is the effective temperature. This latter was derived based on the correspondence with the SpT from M. J. Pecaut & E. E. Mamajek (2013). With the exception of Gaia22efa, Gaia21aul, and Gaia21fji, stellar luminosities do not exceed a few solar luminosities, which aligns with the K−M SpTs determined from both the optical continua and SED fitting.

The stellar masses have been determined by comparing L_* and $T_{\rm eff}$ with the evolutionary tracks of L. Siess et al. (2000). As shown in Figure 15, this comparison typically yields a mass range of 0.25−2.5 $M_{\odot}$ and ages $\lesssim$5 Myr. In the case of Gaia21fji (#15), the data corresponding to the two different distance determinations have been plotted in magenta and red

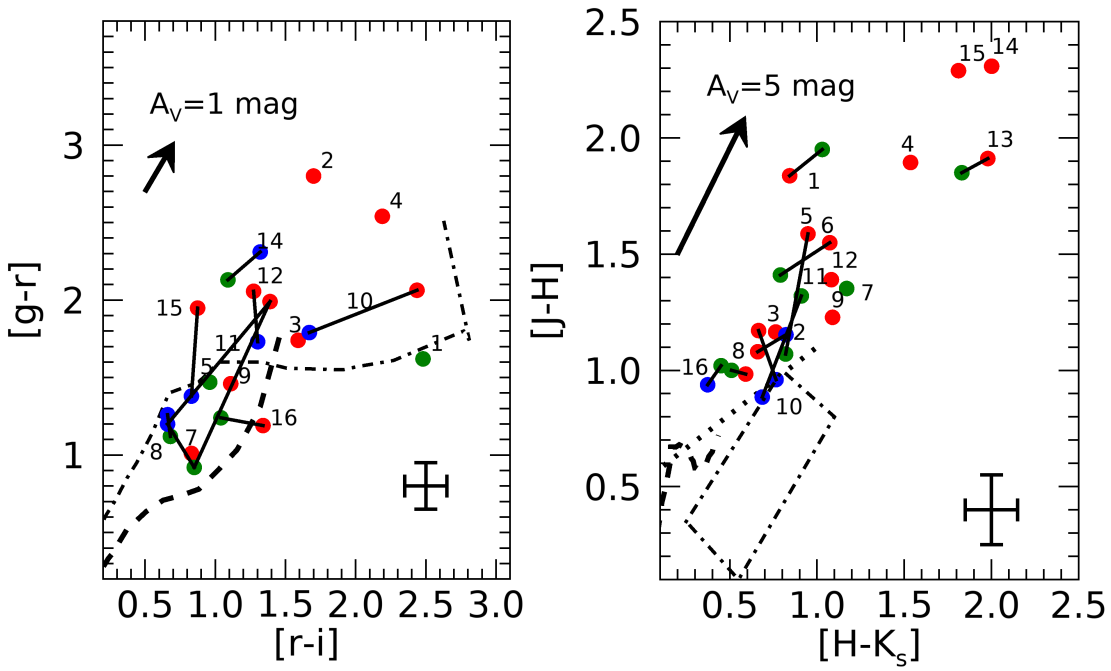

Figure 11. Left panel: two-color $[g-r]$ vs. $[r-i]$ plot. Red, green, and blue dots indicate quiescent, intermediate, and burst data points. Sources are identified by their ID, and black segments connect data from the same source. The dashed–dotted line is the *locus* of young stars with ages of 400–600 Myr (A. L. Kraus & L. A. Hillenbrand 2007), while the dashed line shows the main-sequence stars. The arrow represents the direction of the extinction vector corresponding to $A_V = 1$ mag (reddening law of J. A. Cardelli et al. 1989). In the bottom-right corner, the typical error associated with the data points is shown. Right panel: two-color NIR $[J-H]$ vs. $[H-K_s]$ plot. Color code is the same as in the left panel. The dashed–dotted rectangle is the *l*ocus of unreddened HAeBe stars (J. Hernández et al. 2005), and the dotted line is the *l*ocus of the unreddened T Tauri stars (M. R. Meyer et al. 1997). The arrow indicates the direction of the extinction vector corresponding to $A_V = 5$ mag.

Table 5
Stellar Parameters

ID	Source	α_{2-24}	Class	SpT[a]	$M_{\rm bol}$ ($M_\odot$)	L_* ($L_\odot$)	R_* ($R_\odot$)	M_* ($M_\odot$)	Age (Myr)
1	Gaia21bkw	−0.17	flat	M4 (1)	5.6	0.45 (1)	2.2	0.25 (1)	0.5–1
2	Gaia22efa	−0.47	II	K9	2.5	7.8	6.1	0.65	0.1
3	Gaia22bvi	−0.01 (0.05 (2))	flat	M4 2()	4.4	1.4	2.27 (2)	0.35 (2)	2
4	Gaia22ehn	−0.47	II	M4	5.3	0.6	2.5	0.25	0.5–1
5	Gaia22dbd	−0.34	II	M3–M4[a]	5.9	0.35	1.9	0.25	1–2
6	Gaia21arv	⋯	⋯	K3 (3)	5.0	0.8	1.7	0.9	3
7	Gaia23bri	−0.53	II	K4	4.3	1.4	2.1	1.1	3
8	Gaia21ebu	−0.54	II	K1	3.4	3.4	2.5	1.8	5
9	Gaia21aul	−0.47	II	G1	1.8	15.3	3.6	2.5	5
10	Gaia23bab	−0.57	II	M1 (4)	5.1	0.72 (4)	2.3 (4)	0.4 (4)	1
11	Gaia23dhi	−0.61	II	K2	3.1	4.4	3.0	1.8	3
12	Gaia24afw	−0.81	II	M1	3.4	3.3	4.6	0.4	0.1–0.5
13	Gaia21faq	1.6	I	⋯	>4.8	<0.9	⋯	⋯	⋯
14	Gaia24beh	1.1	I	⋯	>3.2	<4.2	⋯	⋯	⋯
15	Gaia21fji	0.54	I	G0	1.9–0.23	6.4–46	2.3–6.2	2–3.5	1–5
16	Gaia21csu	⋯	⋯	M2	4.3	1.5	3.4	0.35	0.1

Note.
[a] SpT estimated by fitting the SED.
Reference. (1) E. Fiorellino et al. (2021); (2) S. E. Dahm & L. A. Hillenbrand (2020); (3) M. Kounkel et al. (2019); (4) Z. Nagy et al. (2025).

(magenta: $d = 225$ pc; red: $d = 600$ pc). Both sets indicate this is an intermediate-mass object ($M_* = 2-3.5\,M_\odot$) with age $\sim 1-5$ Myr.

7.4. Accretion Luminosity and Mass Accretion Rate

To determine if a source is a genuine EY, it is crucial to quantify its key accretion parameters, namely, the accretion luminosity ($L_{\rm acc}$) and the mass accretion rate ($\dot{M}_{\rm acc}$), during both quiescent and burst phases. A robust method for calculating $L_{\rm acc}$ and $\dot{M}_{\rm acc}$ involves observing lines excited within the accretion columns. For sources where we have optical and/or near-IR spectra, we have estimated $L_{\rm acc}$ based on its correlation with the luminosities ($L_{\rm i}$) of specific accretion lines.

This correlation is defined by the empirical relations ($L_{{\rm acc}(i)}$ versus L_i) established by J. M. Alcalá et al.

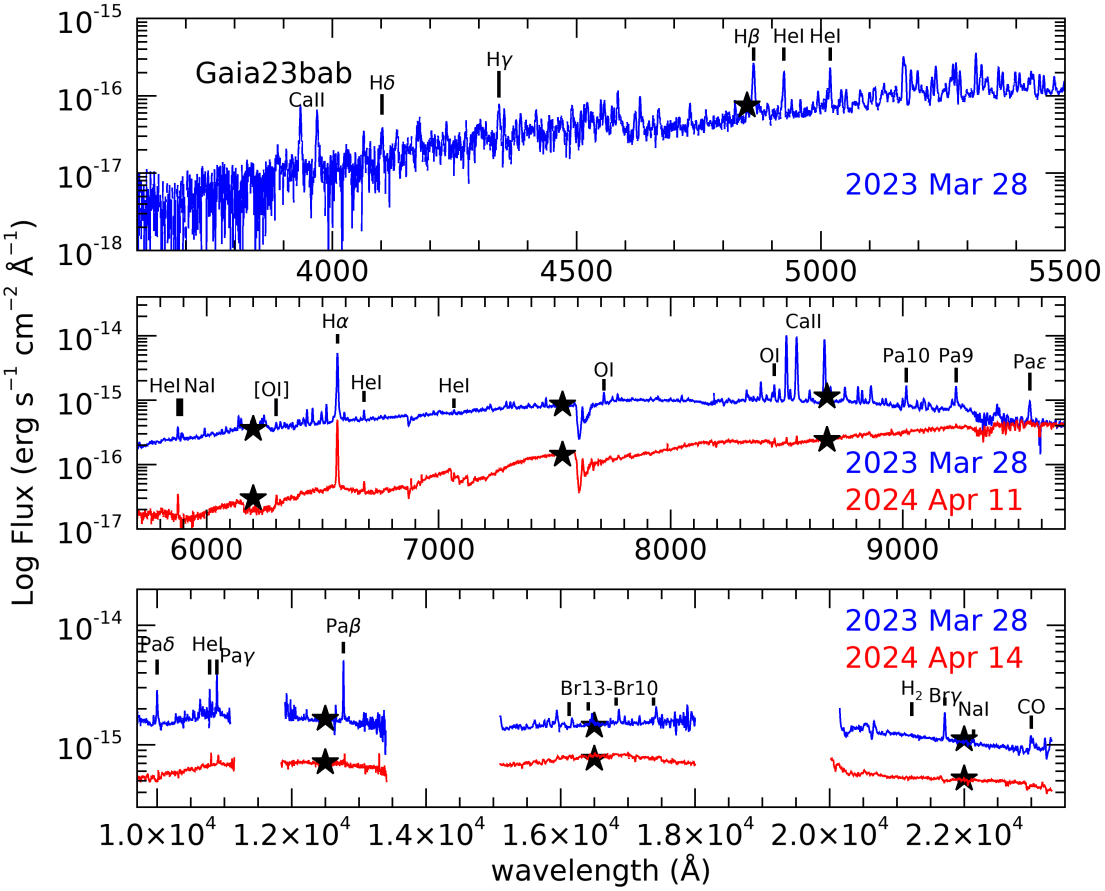

Figure 12. MODS and LUCI spectra of Gaia23bab. Quiescence and burst (T. Giannini et al. 2024) spectra are colored in red and blue, respectively. Observation dates are indicated. Black stars are the photometric points in *grizJHK*$_s$ filters obtained on the same night as the spectrum. The most important detected lines are labeled.

(2017, 2014) for various H I recombination lines from the Balmer, Paschen, and Brackett series, as well as for some He I, O I, and Ca II lines. To determine $L_{\rm acc}$, we have developed a grid of A_V values ranging from 0 to 20 mag (in increments of 0.2 mag). For each A_V value, we calculated the accretion luminosity derived from each line ($L_{{\rm acc}(i)}$). The A_V and $L_{\rm acc}$ (computed as the average of the individual $L_{{\rm acc}(i)}$) pair that yields the minimum dispersion among the $L_{{\rm acc}(i)}$ values is considered the most accurate estimate for these two quantities. We estimate a typical error on A_V within 1.0 mag and on $L_{\rm acc}$ of 0.2−0.3 dex.

With reference to Table 6, we applied the method described above to all the spectra exhibiting accretion lines in emission. The accretion luminosity and mass accretion rate estimates for Gaia21ebu and Gaia23dhi should be considered lower limits due to partial absorption of the H I lines in their spectra. In the case of Gaia21bkw, we get a value for $L_{\rm acc}$ about a factor of 1.5 higher than that estimated by E. Fiorellino et al. (2021). This result is consistent with the source being in a fainter state during the Fiorellino et al. observation period. In particular, their *JHK*$_s$ photometries were approximately 0.2 mag fainter than the LUCI values.

As outlined in Section 2, the majority of our sources have only been observed during a single brightness phase, predominantly during quiescence. Since it is fundamental to measure the variation of $L_{\rm acc}$ across quiescent and burst states, we have estimated $L_{\rm acc}$ using photometric data when spectral data for a particular phase are lacking. In particular, we computed, as representative of $L_{\rm acc,burst}/L_{\rm acc,quiesc}$ the dereddened photometric ratio of $L_{6000,\rm burst}/L_{6000,\rm quiesc}$ between the luminosity at $\lambda \sim 6000$ Å at the burst peak and during quiescence. The photometric bands used are the Gaia *G* band and the ZTF, Pan-STARRS, and MODS *r* band. To validate this procedure, we have applied the same method to sources for which we have line-fitting results, finding agreement within 20%−50%.

In cases where a value for A_V was not available for a specific phase, we have used the average of determinations from other phases. For these cases, our estimate of $L_{\rm acc}$ relies on the assumption that A_V remains constant over time, which may not be accurate. For these sources, obtaining spectra for the missing phase(s) in the future would be beneficial to strengthen the results presented.

Once $L_{\rm acc}$ is derived, the mass accretion rate $\dot{M}_{\rm acc}$ was estimated as

$$\dot{M}_{\rm acc} = (1 - R_*/R_{\rm in})^{-1} L_{\rm acc} R_*/GM_* \quad (4)$$

(E. Gullbring et al. 1998), where $R_{\rm in}$ is the inner-disk radius, assumed $\sim 5R_*$ (L. Hartmann et al. 1998), and *G* is the gravitational constant.

We were able to determine $L_{\rm acc}$ and $\dot{M}_{\rm acc}$ both in quiescence and in outburst for nine sources. The two sources with the most remarkable variability are Gaia21bkw and Gaia23bab, in which $L_{\rm acc}$ and $\dot{M}_{\rm acc}$ increase by more than 2 orders of magnitude. In four

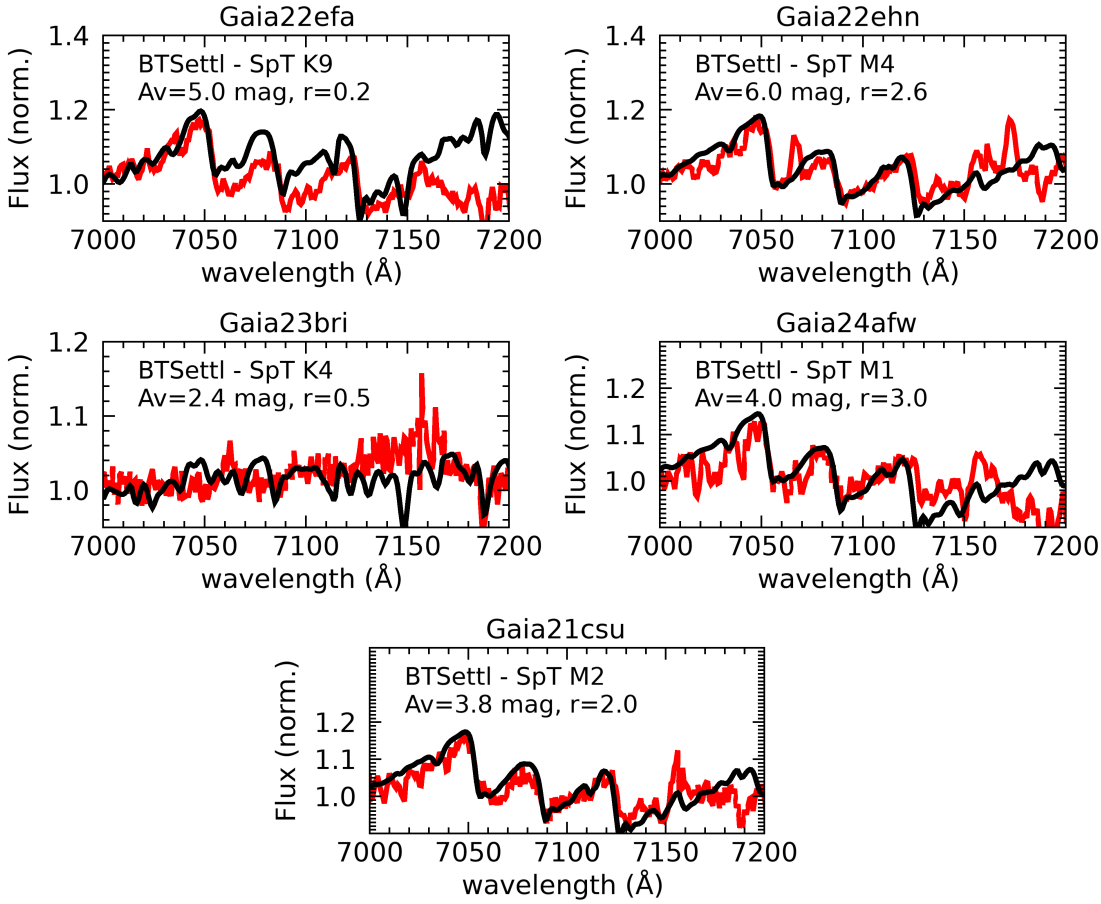

Figure 13. Continuum fitting in the range 7000–7200 Å of quiescence spectra (red). In all panels, the SpT of the best-matching BTSettl model (black), and the fitted A_V and veiling (r) are labeled.

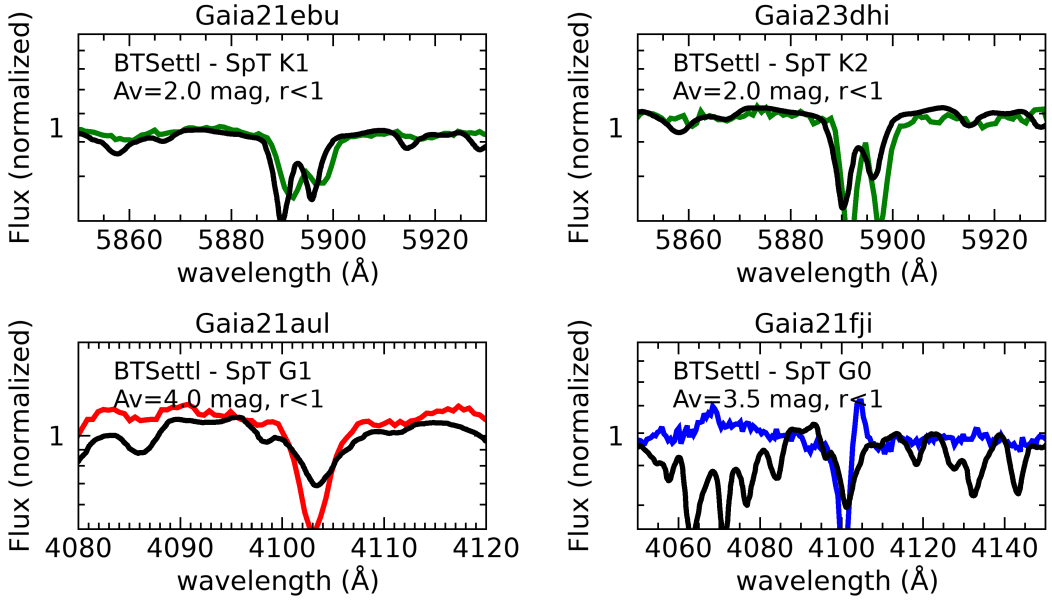

Figure 14. Top: fit of the spectral region around the Na I doublet at 5890 Å in the intermediate state spectra of Gaia21ebu and Gaia23dhi (green). Bottom: fit of the spectral region around the Hγ line for the quiescence spectrum of Gaia21aul (red) and the burst spectrum of Gaia21fji (blue). In all panels, the SpT of the best-matching BTSettl model (black) and the fitted A_V and veiling (r) are labeled.

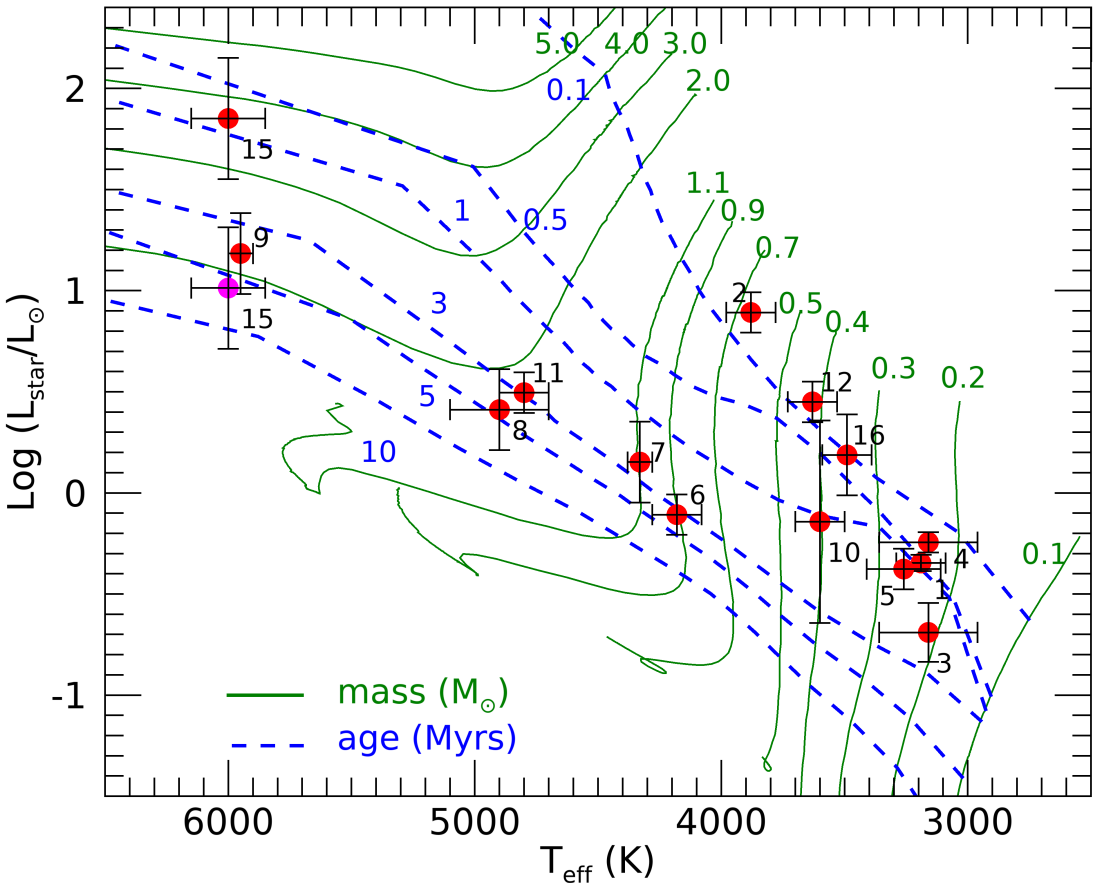

Figure 15. Evolutionary tracks of L. Siess et al. (2000) in the range 0.1−5.0 $M_{\odot}$ (green filled lines) and for ages 0.1−10 Myr (dashed blue lines). The data from the sources of our sample are plotted in red and labeled. In magenta is the point corresponding to the distance estimate of 225 pc for source #15 (Gaia2fji).

Table 6
Accretion Parameters

ID	Source	Quiescence		Intermediate		Outburst	
		log (L_{acc}) ($L_{\odot}$)	log ($\dot{M}_{acc}$) ($M_{\odot}$ yr^{-1})	log (L_{acc}) ($L_{\odot}$)	log ($\dot{M}_{acc}$) ($M_{\odot}$ yr^{-1})	log (L_{acc}) ($L_{\odot}$)	log ($\dot{M}_{acc}$) ($M_{\odot}$ yr^{-1})
1	Gaia21bkw	−2.10 (S)	−8.55 (S)	−0.85 (S)	−7.31 (S)	−0.08 (P)	−6.54 (P)
2	Gaia22efa	−0.36 (S)	−6.79 (S)	⋯	⋯	⋯	⋯
3	Gaia22bvi	−1.13 (S)	−7.71 (S)	⋯	⋯	−0.22 (P)	−6.80 (P)
4	Gaia22ehn	−1.33 (S)	−7.74 (S)	⋯	⋯	0.03 (P)	−6.35 (P)
5	Gaia22dbd	−1.60 (P)	−8.02 (P)	−2.42 (S)	−8.84 (S)	−2.28 (P)	−8.70 (P)
6	Gaia21arv	⋯		−1.28 (S)	−8.45 (S)	⋯	⋯
7	Gaia23bri	−0.80 (S)	−7.92 (S)	−0.34 (S)	−7.20 (S)	0.00 (P)	−7.11 (P)
8	Gaia21ebu	⋯	⋯	>−1.7 (S)	>−8.9 (S)	⋯	⋯
9	Gaia21aul	−0.31 (S)	−7.51 (S)	⋯	⋯	0.41 (P)	−6.79 (P)
10	Gaia23bab	−1.66 (S)	−8.30 (S)	⋯	⋯	0.64 (S)	−5.99 (S)
11	Gaia23dhi	⋯	⋯	>−1.8 (S)	>−9.0 (S)	⋯	⋯
12	Gaia24afw	−0.60 (S)	−6.98 (S)	⋯	⋯	−0.05 (P)	−6.43 (P)
13	Gaia21faq	⋯	⋯	0.07 (S)		0.22 (P)	⋯
14	Gaia24beh	⋯	⋯	⋯	⋯	2.00 (S)	⋯
15	Gaia21fji[g]	⋯	⋯	⋯	⋯	0.17[a]–1.07[b] (S)	−7.26[a] to −6.13[b] (S)
16	Gaia21csu	−1.7 (S)	−8.1 (S)	−1.62 (S)	−8.0 (S)	−1.30(P)	−7.71 (P)

Notes. In parentheses is indicated the method used to derive the A_V: S: spectroscopy, P: photometry.
[a] Computed assuming $d = 225$ pc.
[b] Computed assuming $d = 600$ pc.

Table 7
Light-curve Analysis

Source	ΔG/ΔW1 (mag)	Maximum Amplitude (mag)	Gaia Peaks	Average Duration (days)	Ris./Decl. Speed (mmag day^{-1})	Group
Gaia21bkw	2.2/2.9	2.3	5	284	14/10	A
Gaia22efa	1.1/0.5	1.5	1	530	20/9.5	A
Gaia22bvi	2.1/1.2	2.3	5[a]	273	13/12	A
Gaia22ehn	2.9/2.7	4.2	3[b]	180	27/22	B
Gaia22dbd	1.3/0.5	3.4	1	362	9/40	B
Gaia21arv	1.3/0.5	2.2	3	637	2.5/4	B
Gaia23bri	2.1/0.5	3.4	5	375	11/10	B
Gaia21ebu	1.2/0.9	2.0	1	324	8/7	B
Gaia21aul	1.0/0.7	2.9	1	551	3/9	B
Gaia23bab	2.3/1.4	2.6	2[c]	589	11/8	A
Gaia23dhi	1.6/0.8	3.0	…	…	…	B
Gaia24afw	0.9/0.3	1.2	2	106	16/18	A
Gaia21faq	1.4/1.2	2.5	3	336	6/3	B
Gaia24beh	2.0/1.0	3.9	…	…	…	B
Gaia21fji	2.0/1.0	2.8	…	…	…	B
Gaia21csu	2.1/1.0	3.3	3	372	10/11	B

Notes. ΔG: G_{peak}–G_{median}; ΔW1: $W1_{peak}$–$W1_{median}$; maximum amplitude: G_{min}–G_{max}; average duration: time elapsed between two subsequent quiescent levels; rising/declining speed: time elapsed from quiescence to peak and viceversa.
[a] Two peaks detected by ZTF.
[b] One peak detected in W1/W2.
[c] A further peak was detected by Pan-STARSS in 2013, just before the beginning of the Gaia mission.

sources (Gaia22bvi, Gaia22ehn, Gaia23bri, and Gaia21aul), L_{acc} and $\dot{M}_{acc}$ vary by factors between 5 and 30, while in two objects, Gaia24afw and Gaia21csu, the variation is lower than a factor of 3. In Gaia22dbd, the observed variability appears to be due to extinction rather than accretion variability ($\Delta A_V \sim 6$ mag). Indeed, the intrinsic accretion luminosity during a burst is even lower than what is measured during the quiescent phase. Similarly, variable extinction may also play a role in the variability observed in Gaia21csu, since A_V decreases by approximately one magnitude between the quiescent and burst phases.

8. Discussion

8.1. Light-curve Analysis

In Section 4, we presented the light curves for each source in our sample, as shown in Figures 3–6. We now broaden our discussion on these light curves, emphasizing the similarities and differences we observed throughout the 10 yr Gaia dataset. One particularly interesting feature is the significant diversity in light curves, even among sources with comparable mass, age, and luminosity. This likely indicates that the mechanisms responsible for the observed variability are inherently varied and influenced by multiple factors.

From a visual inspection of Figures 3–6, we can note that our sources can be broadly categorized into two main groups (Table 7). The first group ("A") includes light curves displaying distinct peaks above a relatively stable baseline, such as the EXor source Gaia23bab. The second group ("B") consists of sources displaying significant variability throughout the observation period, with some never achieving a stable state. This variability manifests in several ways, including irregular brightness fluctuations, dips, low-frequency modulation, or a continuous increase in brightness starting from a specific date with superposed higher-frequency variability. Alongside accretion variability, we observe low-amplitude variations with timescales of days, which likely originate from stellar activity and rotation, as well as regular or abrupt changes in extinction, potentially caused by warps, clumps within the disk, or geometrical effects (J. Bouvier et al. 2007; L. Venuti et al. 2015).

It is also noteworthy that the mid-IR light curve does not always consistently reflect the trends seen in the Gaia data. For example, the W1/W2 light curve of Gaia22bvi shows a low-frequency modulation that is not present in the *G*-band data. Similarly, for Gaia22ehn, a burst detected in W1/W2 during 2018 has no counterpart in the *G* light curve. In the cases of Gaia21arv and Gaia23dhi, brightness increases in the *G* band align with minima in W1/W2, while a burst detected in 2016 April in Gaia21ebu corresponds to a low-frequency rising and decreasing in the W1/W2 light curve.

As a general observation, we note that the wide variety we see in the Gaia light curves is not reflected in the optical and IR spectra, which all display the same emission lines. Similarly, the SEDs across our sample are uniformly characteristic of YSOs.

To identify common features and properties within the light curves, we conducted a more quantitative analysis, the results of which are presented in Table 7. To account for the fluctuations seen in the optical (*G*) and mid-IR (W1) light curves across different sources, we applied our analysis method to both the Gaia and NEOWISE datasets. First, to minimize the influence of outliers and burst events, we have taken as the Gaia brightness baseline the median magnitude (G_{median}) during the 10 yr of the operations. Then, we identified a "Gaia peak" (G_{peak}) as any event where the brightness, sampled by at least two photometric measurements, increased by at least one magnitude compared to the baseline level ($\Delta G = G_{peak} - G_{median} \gtrsim 1$). Analogously, we have defined the peaks in the W1 band. Finally, we note that a similar analysis performed on the *r*-band ZTF data reveals

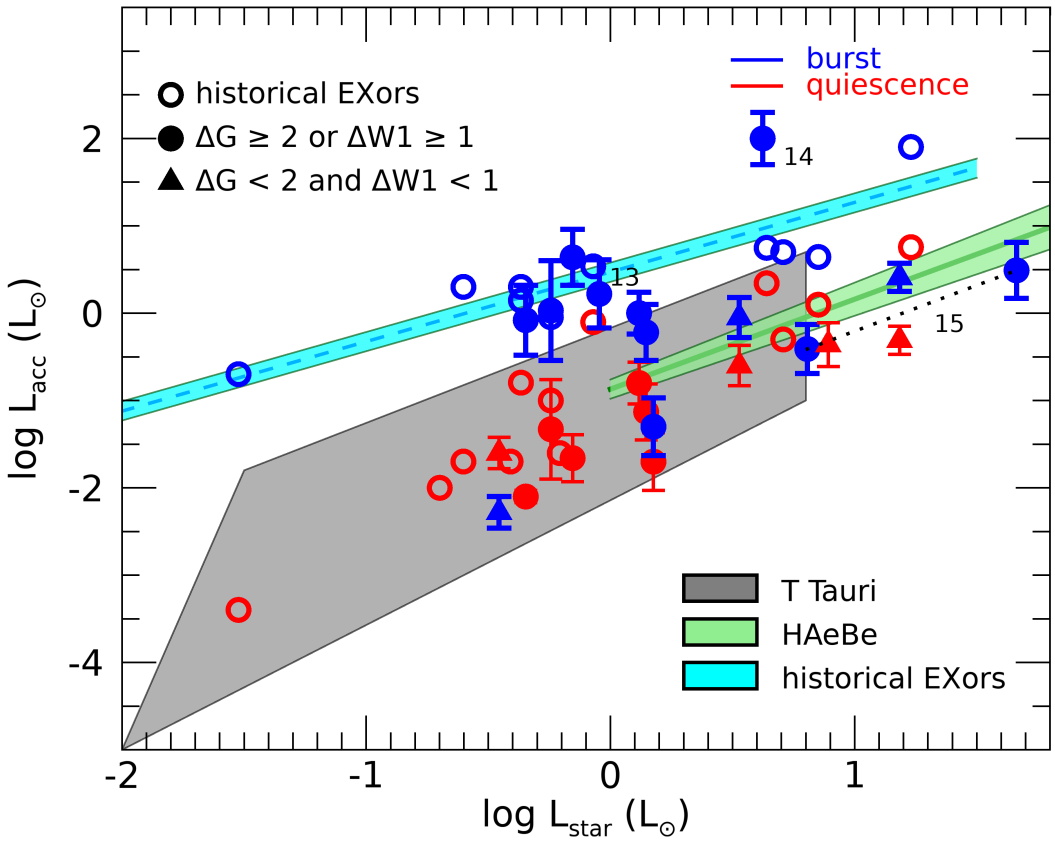

Figure 16. L_{acc} vs. L_*. Sources in quiescence and in burst are colored in red and blue, respectively. Filled circles are sources with $\Delta G \gtrsim 2$ or $\Delta W1 \gtrsim 1$, while triangles are sources with $\Delta G < 2$ and $\Delta W1 < 1$. Gray and green shaded areas represent the *loci* of T Tauri (C. F. Manara et al. 2021) and HAeBe stars (C. Wichittanakom et al. 2020). The blue dotted line and the shaded area are the fit through a sample of historical EXor bursts (T. Giannini et al. 2024), plotted with blue (burst) and red (quiescence) open circles. The three Class I sources are indicated with their identification number, and the dotted line connects the data of source #15 for the two distance determinations.

the same peaks found with the Gaia data. The only exception is the presence of two additional peaks detected in the Gaia22bvi light curve between 2018 and 2019, during which no Gaia observations were performed.

The identified peaks are visually represented in Figures 3–6 with a thick red line. We underline that our definition excludes episodes of strong irregular variability, as well as phenomena characterized by a gradual increase in brightness or a sustained period of high brightness, as observed, for example, in Gaia22efa and Gaia21ebu. We classify as "very active" objects exhibiting at least an episode of brightness increase with $\Delta G \gtrsim 2$ mag or $\Delta W1 \gtrsim 1$ mag, assuming that the amplitude of the variation decreases with the wavelength (e.g., D. Lorenzetti et al. 2007). As shown in the second column of Table 7, these are Gaia21bkw, Gaia22bvi, Gaia22ehn, Gaia23bri, Gaia23bab, Gaia21faq, Gaia24beh, Gaia21fji, and Gaia21csu. According to the α values and ages presented in Table 5, this group of "very active" objects includes the three Class I and the two flat-spectrum sources, along with three Class II sources, almost all with ages $\lesssim$2 Myr. Conversely, the "less active" group is composed of six Class II sources, along with one source that has an unknown spectral index. These sources have ages ranging from 2 to 5 Myr, with the exception of Gaia22efa and Gaia24afw, which have ages less than 0.5 Myr. Gaia22efa, however, might be more active than one can think on the basis of its 10 yr light curve, as demonstrated by the steep rise in brightness occurring since last year.

We also report in Table 7 the maximum amplitude (G_{min}–G_{max}) in the Gaia light curve. When this value does not exceed ΔG by more than 10%–30%, the light curve has a relatively constant baseline. Conversely, the light curve may exhibit irregular variability, dips, or a nonflat slope. As said, this latter case involves the majority of our sources. Another interesting aspect to consider is the frequency of enhanced brightness events. Notably, the objects categorized as "very active" also experience peaks of brightness more frequently, typically with three to five peaks in 10 yr. Conversely, with a couple of exceptions, the light curves of less active objects display just one peak.

Our analysis indicates that the burst duration generally falls between 200 and 600 days, and that both the rising and the declining speed are from a few to a dozen millimagnitudes per day, with no significant difference observed between the more and less active source groups. This result is confirmed from the analysis of the ZTF light curves, whose optimal ∼2 day cadence is more suited for accurately capturing events with durations comparable to the sampling frequency.

8.2. Accretion versus Stellar Parameters

In this section, we will discuss the parameters derived from the emission lines, specifically the accretion luminosity and the

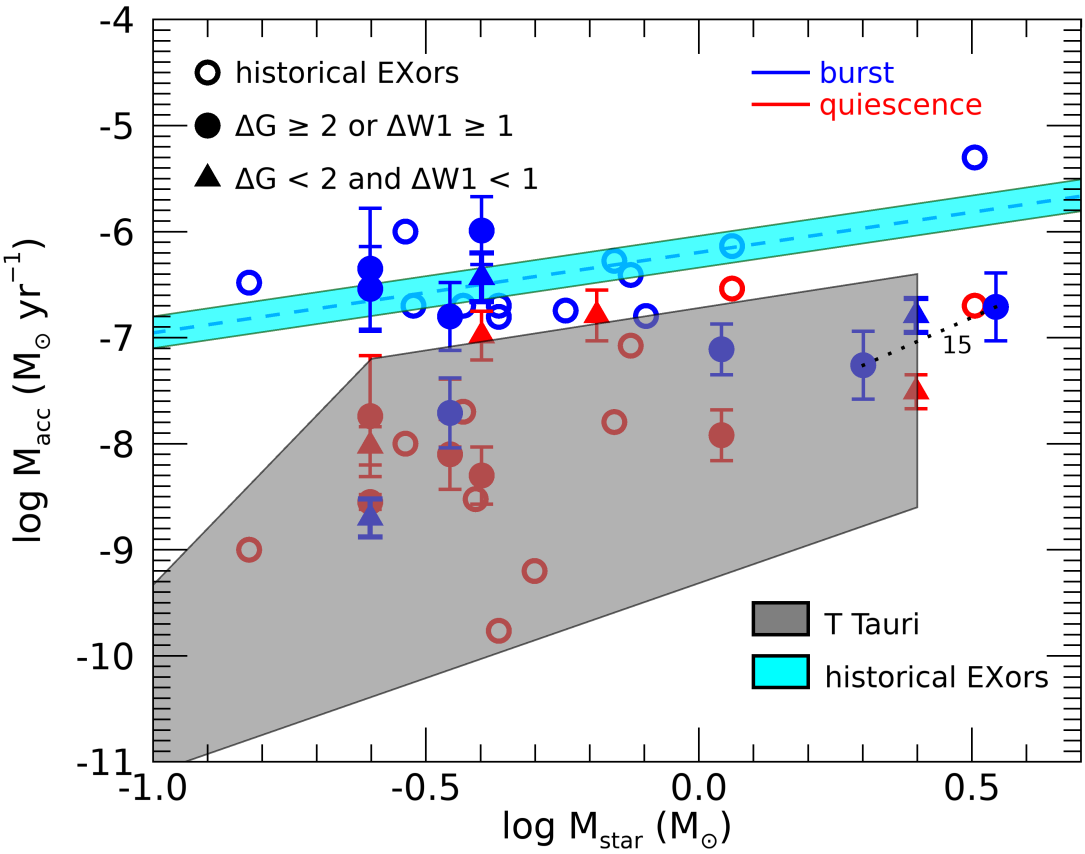

Figure 17. $\dot{M}_{\rm acc}$ vs. M_*. Colors and symbols have the same meaning as in Figure 16.

mass accretion rate. Figure 16 shows $L_{\rm acc}$ versus L_* for the quiescence (red) and burst (blue) phases of the sources in our sample. The most active sources are represented by filled circles, while others are shown with filled triangles. For comparison, the *loci* of accreting T Tauri stars in several star-forming regions (C. F. Manara et al. 2021) and HAeBe stars (C. Wichittanakom et al. 2020) are displayed as gray and green shaded areas, respectively. The dashed cyan line and shaded area represent the fit through a sample of nine historical EXors during burst (T. Giannini et al. 2024), shown with blue open circles. Additionally, quiescence data for 12 known EXors are plotted with red open circles.

From this plot, we note several features: (1) When in quiescence, all our sources, as well as known EXors, occupy the same parameter space as T Tauri or HAeBe stars. (2) The variability observed in "less active" sources is consistent with that seen in T Tauri stars. (3) During a burst, four of the nine "very active" sources lie within the *locus* of EXor bursts, and two are at the upper end of the *locus* of T Tauri sources. (4) The position of the Class I Gaia24beh (#14) is noteworthy, as its $L_{\rm acc}$ value is approximately 1 order of magnitude above the location of the EXor bursts. The Class I object Gaia21faq (#13) is within the *locus* of the EXors, while the $L_{\rm acc}$ of the other Class I source Gaia21fji (#15) appears consistent with an HAeBe star.

The plot of $\dot{M}_{\rm acc}$ versus M_* shown in Figure 17 supports conclusions similar to those drawn from the $L_{\rm acc}$ versus L_* plot. In particular, all sources in their quiescent state are located within the parameter space of the T Tauri sources. During bursts, the "very active" objects are found to be on or slightly below the *locus* of EXor bursts, although with some exceptions. Unfortunately, we were unable to compute M_* for the two Class I Gaia24beh and Gaia21faq, due to a lack of data needed to derive their SpT and related parameters. For Gaia21fji, our estimates suggest values characteristic of intermediate-mass objects.

From our analysis, we can draw two main conclusions. First, sources showing photometric variations of approximately 2 mag in the optical are strong EY candidates. Second, when these objects are in quiescence, they do not show significant differences from classical T Tauri or HAeBe stars. Although our statistical sample is small, this finding supports the idea that all low- and intermediate-mass objects *may potentially* experience significant episodes of burst accretion. This variability could therefore be a key process contributing to the considerable spread observed in the relations between accretion and stellar parameters.

9. Summary and Conclusions

This paper presents the 10 yr light curves and optical/near-IR spectroscopic LBT follow-up for a sample of 16 sources alerted by Gaia between 2021 and 2024 (eight known YSOs and eight YSO candidates). While our study was based on a small statistical sample and observations were limited by unfavorable atmospheric conditions and technical issues, we were able to achieve several key results, which are summarized below.

1. In terms of spectral index, the sample is composed of three Class I sources, two flat-spectrum sources, nine Class II sources, and two sources with unknown class.
2. The light curves of our sample can be classified into two distinct groups: those with clear peaks above a stable baseline (Gaia21bkw, Gaia22efa, Gaia22bvi, Gaia23bab, and Gaia24afw) and those exhibiting significant variability across the entire observation period (Gaia22ehn, Gaia22dbd, Gaia21arv, Gaia23bri, Gaia21ebu, Gaia21aul, Gaia23dhi, Gaia21faq, Gaia24beh, Gaia21fji, Gaia21csu). This complex nature of the light curves suggests that multiple processes likely contribute to the observed variability.
3. All sources display an SED characteristic of a YSO. In particular, they show a peak in the near-IR or even at longer wavelengths, along with a significant IR excess. These characteristics strongly support the classification as genuine YSOs of the eight objects classified by Gaia as "YSO candidates."
4. Color–color diagrams indicate that the observed variability in most of the sources is primarily due to episodes of enhanced accretion, with changes in extinction playing a minor role.
5. The spectra show characteristics typical of YSOs, specifically a rising continuum in the optical range and the presence of emission lines. It is particularly notable that over half of the spectra display atomic forbidden lines. These lines are key indicators of gas in ejection, which is tightly linked to ongoing accretion.
6. We have derived the stellar parameters for most of our sources through the analysis of the continuum, emission lines, and SED. With the exception of Gaia21aul and Gaia21fji, which are intermediate-mass stars, our sample primarily consists of low-mass objects with SpT K–M, and ages from 0.1 to 5 Myr.
7. From the analysis of the light curves, we have identified as "very active" objects those exhibiting at least an episode of brightness increase with $\Delta G \gtrsim 2$ mag, or $\Delta W1 \gtrsim 1$ mag. These sources not only show outbursts with the largest amplitudes but also experience brightness peaks more frequently, typically from three to five peaks within a 10 yr period. This group includes the three Class I sources and the two flat-spectrum sources.
8. We have derived the accretion luminosity and the mass accretion rate in various phases of brightness from the luminosities of the accretion lines. For nine sources, we were able to determine these quantities during both quiescence and burst phases. In particular, for Gaia21bkw and Gaia23bab, we observed an increase in accretion luminosity and mass accretion rate of more than 2 orders of magnitude during burst phases. In two sources (Gaia22dbd and Gaia21csu), the observed variability is likely mainly attributable to extinction variations. For the remaining sources, the increase in accretion parameters typically ranges from a factor of 5–30.
9. The plot $L_{\rm acc}$ versus L_* reveals that all our sources, when in quiescence, occupy the same parameter space as T Tauri or HAeBe stars. This result supports the idea that all low- and intermediate-mass objects may experience significant episodes of burst accretion.
10. When in burst, the "very active" sources fall in the parameter space of EXor bursts or close to the upper end of the T Tauri *locus*, therefore being strong EY candidates. Notably, the Class I Gaia24beh exhibits an exceptionally high accretion luminosity, approximately an order of magnitude greater than EXors of comparable mass. Furthermore, the $\dot{M}_{\rm acc}$ versus M_* relation supports conclusions consistent with those drawn from the $L_{\rm acc}$ versus L_* relation.

A significant advancement in our understanding of YSO variability is expected with the upcoming Legacy Survey on Space and Time (LSST[24]), conducted by the Vera C. Rubin Observatory. The Rubin LSST's rapid cadence and high sensitivity will allow for systematic coverage and monitoring of most known star-forming regions. When combined with spectroscopic monitoring from instruments like X-Shooter and SoXS at ESO, these observations will offer an unprecedented opportunity to determine the percentage of eruptive variables, especially in regions of moderate extinction.

Acknowledgments

We acknowledge ESA Gaia, DPAC, and the Photometric Science Alerts Team (http://gsaweb.ast.cam.ac.uk/alerts). This work has made use of data from the European Space Agency (ESA) mission Gaia (https://www.cosmos.esa.int/gaia), processed by the Gaia Data Processing and Analysis Consortium (DPAC; https://www.cosmos.esa.int/web/gaia/dpac/consortium). Funding for the DPAC has been provided by national institutions, in particular the institutions participating in the Gaia Multilateral Agreement. We acknowledge support from the Large Grant INAF 2022 "YSOs Outflows, Disks and Accretion: toward a global framework for the evolution of planet forming systems (YODA)" and from PRIN-MUR 2022 20228JPA3A "The path to star and planet formation in the JWST era (PATH)." This project has received funding from the European Research Council (ERC) via the ERC Synergy Grant ECOGAL (grant 855130). Views and opinions expressed are, however, those of the author(s) only and do not necessarily reflect those of the European Union or the European Research Council Executive Agency. Neither the European Union nor the granting authority can be held responsible for them. We acknowledge the Hungarian National Research, Development and Innovation Office grant OTKA FK 146023. We acknowledge support from the ESA PRODEX contract No. 4000132054. Z.N. was supported by the János Bolyai Research Scholarship of the Hungarian Academy of Sciences. This research has made use of the Spanish Virtual Observatory (https://svo.cab.inta-csic.es) project funded by MCIN/AEI/10.13039/501100011033/ through grant PID2020-112949GB-I00.

Appendix A
Notes on the Individual Sources

In this Appendix, we give some notes on the individual sources. In particular, we report on: (a) distance determination with reference to Figures 1–2; (b) brightness level at the epoch of the LBT observation; (c) notes to the individual SED, with reference to Figures 7−10.

Gaia21bkw (a) Distance taken from the literature.
(b) Observed with LBT twice, once during quiescence and once in an intermediate state.

[24] https://rubinobservatory.org/

(c) SED with excess at wavelengths $\gtrsim 8\,\mu$m. The LBT photometric data in its quiescent state align well with the 2MASS, AllWISE, and Spitzer datasets. Furthermore, the data from the intermediate state show good agreement with the ZTF data. We also observe a blue excess. Notably, the Gaia photometric point during the burst phase does not match any other data points. A BB function with $T_{\rm eff} = 3190$ K (as reported by E. Fiorellino et al. 2021), when reddened by $A_V = 9.8$ mag, provides a good fit to the quiescence photometric points across the optical to the mid-IR range (Figure 7, panel (a)).

Gaia22efa (a) This star is in the Auriga–California Molecular Cloud at a distance between 450 and 510 pc. The source has a large distance of 922^{+619}_{-187} pc from C. A. L. Bailer-Jones et al. (2021, BJ21), and has a high RUWE of 2.29. The cluster NGC_1579 from E. L. Hunt & S. Reffert (2024) has a median distance of 521 pc, while the extinction rises at 532 pc. We adopt this latter value as the distance to Gaia22efa.

(b) Object observed during quiescence.

(c) The SED shows a notable excess at wavelengths greater than 3.4 μm (Figure 7, panel (b)). The LUCI photometric data points are lower than the 2MASS data, which suggests a previous high brightness level that has not been observed since 2014. The BB function with $T_{\rm eff} = 3900$ K, reddened by $A_V = 5.0$ mag (as determined from the continuum fitting), provides a reasonable fit to the quiescent photometric data points across the optical to near-IR spectrum.

Gaia22bvi (a) Distance taken from the literature.

(b) Object observed in quiescence.

(c) The SED extends up to 160 μm based on Akari data and exhibits an excess at wavelengths longer than approximately 2.2 μm (as shown in Figure 7, panel (c)). Our continuum fit indicates $A_V = 3.2$ mag and $T_{\rm eff} = 3200$ K, which aligns with the findings of S. E. Dahm & L. A. Hillenbrand (2020). A BB function accurately fits the quiescent data from the optical range up to the K-band photometry. Additionally, burst data are available from the Gaia, ZTF, and NEOWISE surveys.

Gaia22ehn (a) The source is located in LDN 1536 in Taurus. We adopt the value estimated by Z. Nagy et al. (2025, in preparation) of 152 pc.

(b) Object observed in quiescence.

(c) The SED extends up to 160 μm (Akari data), showing excess at $\lambda \gtrsim 1.6\,\mu$m (Figure 7, panel (d)). The BB fits nicely the optical and near-IR photometries, $T_{\rm eff} = 3200$ K and $A_V = 6.0$ mag being derived from continuum fitting. The SED extends up to 160 μm based on Akari data and exhibits an excess at wavelengths longer than approximately 1.6 μm (as shown in Figure 7, panel (d)).

Gaia22dbd (a) We adopt the BJ21 distance of 345^{+7}_{-5} pc, which matches that of Orion, where the source is located.

(b) This object was observed during an intermediate state of brightness.

(c) The photometric data in the SED (Figure 8, panel (a)) correspond to four distinct brightness levels of the source. As can be seen, both blue and red excesses are present. In particular, the 2MASS data were acquired when the source was at its faintest state, and were specifically used by means of the $[J-H]$ and $[H-K_s]$ colors to determine $A_V = 7.0$ mag during quiescence. $T_{\rm eff}$ has been estimated from the SED fit with a significant degree of uncertainty.

Gaia21arv (a) The photogeometric distance is in agreement with that of Orion, where the object is located. The distance of 390 ± 12 pc is in agreement with the cluster NGC_1980.

(b) This object was observed solely with LUCI during a period of intermediate brightness. However, this brightness level does not appear to significantly exceed the 2MASS data points, which characterize its quiescent state.

(c) The SED shows a moderate excess that sharply decreases at mid-IR wavelengths (Figure 8, panel (b)). Our continuum fit yields $T_{\rm eff} = 4180$ K, which aligns with the findings of M. Kounkel et al. (2019). The optical and J-band data are well-fitted by a BB function with a reddening of $A_V = 6.0$ mag, consistent with the near-IR colors. Additionally, the ZTF g-band photometry indicates a blue excess.

Gaia23bri (a) Its BJ21 distance is 1974^{+671}_{-396} pc, and its RUWE is 1.04. The proper motions in Figure 1 suggest it can be a member of HSC_1421. Its median distance is 1514 pc. The spatial distribution and lower distance uncertainty also strengthen this idea. The extinction rises at 1586 pc, which we adopt as the distance.

(b) For this source, we have an optical/near-IR spectrum in quiescence and a near-IR spectrum obtained when the source was in an intermediate brightness state, with magnitudes similar to those observed by 2MASS.

(c) This SED (Figure 8, panel (c)) displays a remarkable IR excess. A $T_{\rm eff} = 4330$ K and $A_V = 2.4$ mag, as derived from the continuum fitting in quiescence, are used to plot the BB function, normalized to the LUCI datum obtained in quiescence. This function is slightly above MODS and Pan-STARRS data points, maybe because the source was brighter at the time of LUCI observations.

Gaia21ebu (a) The BJ21 distance is 1383^{+199}_{-164} pc. It is inside the Rosette Nebula ($d \sim 1300$ pc), so the distance is in agreement with its location. The distance histogram agrees with the adopted distance as well.

(b) The source was observed in an intermediate state that shows little difference from both its quiescent and burst phases.

(c) The source exhibits an excess primarily in the AllWISE data at $\lambda \gtrsim 10$ m. A BB function, reddened by $A_V = 3.0$ mag as determined from

the near-IR colors, provides the best fit to the quiescence points for a temperature $T_{\rm eff} = 4900$ K (as shown in 8, panel (d)).

Gaia21aul (a) The distance of 379^{+12}_{-11} pc from BJ21 aligns with the distance distribution of UPK_39 members.
(b) This object was observed during quiescence.
(c) The SED shows an excess extending up to 160 μm, based on Akari data. Our continuum fitting indicates $T_{\rm eff} = 5950$ K and $A_V = 4.0$ mag. The reddened BB function effectively fits the optical (Gaia, ZTF, and MODS) and near-IR data. However, the Pan-STARRS data points are notably below the other observations, a trend also visible in the light curve. These data points can be accurately fitted using the same BB function, provided it is reddened by an A_V of approximately 5 mag (Figure 9, panel (a)).

Gaia23bab (a) Distance taken from the literature.
(b) This source was observed both in quiescence and in bursts.
(c) The SED in burst is already described in T. Giannini et al. (2024), while in this paper, we present data obtained in quiescence (Figure 9, panel (b)). The continuum fitting of the quiescence data provides $T_{\rm eff} = 3630$ K and $A_V = 3.2$ mag. The reddened BB function fits the Gaia, MODS, LUCI, and 2MASS data. ZTF and Pan-STARRS photometries are below the fit, possibly due to source variability across the different surveys.

Gaia23dhi (a) The photogeometric distance and the position angle of the proper motion vector suggest it is a member of HSC_432. We adopt the BJ21 distance of 2735^{+638}_{-451} pc.
(b) This object was observed during an intermediate state of brightness.
(c) The photometric data probe three distinct brightness levels, with the 2MASS data specifically representing the highest (Figure 9, panel (c)). Through continuum fitting, we have estimated $T_{\rm eff} = 4800$ K. The BB at this temperature, reddened by $A_V = 3.0$ mag (as determined from near-IR colors), provides a good fit to the optical Gaia, Pan-STARRS, and ZTF data. We have normalized this BB function using the photometric point in the J band obtained with LUCI.

Gaia24afw (a) Although the proper motion slightly differs from that of the cluster NGC_6823, the distance suggests it is a member of it. We use the BJ21 distance of 2150^{+973}_{-570} pc.
(b) This object was observed during quiescence.
(c) The SED shows a peak around 3 μm, followed by a decline in the mid-IR range, where a noticeable excess is present (Figure 9, panel (d)). Our fit to the optical continuum indicates $T_{\rm eff} = 3630$ K and $A_V = 4.0$ mag. We have used these values to plot the reddened BB function, which provides a good fit through all the optical data.

Gaia21faq (a) The star is in the Cygnus X SFR at 1400 pc, which falls in the range of values from BJ21 (1190^{+474}_{-258} pc).
(b) This object has been observed during an intermediate state of brightness.
(c) The SED shows a steep increase with wavelengths up to approximately 3 μm, followed by a plateau at longer wavelengths (Figure 10, panel (a)). The spectral index suggests that this is a Class I object. Analysis of 2MASS photometry indicates that Gaia21faq was in a fainter state about 30 yr ago compared to its current brightness. Data from Pan-STARRS, ZTF, LBT, and AllWISE are consistent with each other, showing an intermediate brightness level relative to the peak of the Gaia light curve. The 2MASS colors indicate $A_V = 5.0$ mag. A similar value is obtained from continuum fitting, suggesting that the extinction did not significantly change during the different brightness phases observed. No BB fit was performed.

Gaia24beh (a) The spatial distribution shows that this source can be located on the edge of the cluster UPK_127. We use the distance 741^{+17}_{-15} pc from BJ21.
(b) Source observed during burst.
(c) The 2MASS data reveal a considerably fainter brightness phase for Gaia24beh compared to what has been observed over the following three decades, similar to the case of Gaia21faq. As illustrated in Figure 10 (panel (b)), the SED exhibits a steep increase toward longer wavelengths, classifying Gaia24beh as a Class I source. The near-IR color–color diagram in quiescence indicates an extinction of 10 mag, which is higher than the value of 5.2 mag estimated from continuum fitting in the burst. This discrepancy suggests that a variation in extinction plays a part in the observed brightening. No BB fit was performed.

Gaia21fji (a) The star is located toward Cygnus-L988, a cloud that supposedly has a distance of 600 pc, which aligns with both the peak of the histogram of LDN_988e and the extinction increases at 626 pc. The BJ21 distance is 225^{+22}_{-18} so it is separated from the other two estimates. We will adopt both the distances (Z. Nagy et al. 2025, in preparation).
(b) This object was observed during a burst.
(c) The photometric data of Gaia21fji suggest it is a Class I source (Figure 10, panel (c)). The quiescent data are fitted by a BB at $T = 6000$ K reddened by $A_V = 10.0$ mag, in agreement with the SpT derived from the 370 to 450 nm fitting and the A_V obtained from the near-IR color–color diagram.

Gaia21csu (a) This star is in LDN 1218. The extinction rises at 856 pc, which aligns with the BJ21 distance of 834^{+93}_{-78}.
(b) This source was observed during quiescence with MODS and in an intermediate state with MODS and LUCI.
(c) In the SED (Figure 10, panel (d)), we observe an excess at $\lambda \gtrsim 4.4$ μm. Our continuum fitting indicates $T_{\rm eff} = 3500$ K and $A_V = 3.8$ mag, which fits most of the optical data.

Appendix B
LBT Photometry

In this Appendix, we show the tables of the optical (*griz*) and near-IR (JHK_s) magnitudes obtained with MODS and LUCI (Tables 8 and 9, respectively).

Table 8
Optical Photometry

ID	Source	Date	g	r	i	z
1	Gaia21bkw	2023 Mar 5	>20.4[a]	18.78	16.3[a]	14.9[a]
2	Gaia22efa	2023 Oct 17	18.8	16.0	14.3	13.0
3	Gaia22bvi	2023 Oct 19	16.46	14.72	13.13	12.02
4	Gaia22ehn	2023 Oct 19	20.19	17.65	15.46	14.33
5	Gaia22dbd	2024 Jan 10	17.10	15.63	14.67	14.08
7	Gaia23bri	2023 Oct 19	18.62	17.61	16.78	16.06
8	Gaia21ebu	2024 Jan 10	16.75	15.63	14.95	14.47
9	Gaia21aul	2023 Jun 4	14.59	13.13	12.02	11.31
10	Gaia23bab	2024 Apr 11	…	19.80	17.46	16.44
11	Gaia23dhi	2024 Jun 7	18.22	17.30	16.45	15.88
12	Gaia24afw	2024 Jun 7	20.41	18.78	17.49	16.70
13	Gaia21faq	2023 Jun 4	…	18.39	17.24	16.38
14	Gaia24beh	2024 Jun 8	18.00	15.69	14.37	13.51
15	Gaia21fji	2023 Oct 19	15.99	14.61	13.78	13.13
16	Gaia21csu	2022 Dec 17	17.51	16.27	15.23	14.78
		2023 Oct 19	18.86	17.77	16.33	15.35

Notes. Errors are within 0.1 mag.
[a] Taken from the ZTF catalog.

Table 9
IR Photometry

ID	Source	Date	J	H	K_s
1	Gaia21bkw	2021 Oct 15	13.61	11.83	10.88
		2023 Feb 28	12.48	10.53	9.50
2	Gaia22efa	2023 Nov 23	10.92	9.84	9.18
3	Gaia22bvi	2023 Nov 22	9.81	9.10	8.58
5	Gaia22dbd	2024 Jan 9	12.60	11.53	10.71
6	Gaia21arv	2021 Oct 15	12.74	11.31	10.44
7	Gaia23bri	2023 Nov 23	14.53	…	…
		2024 Jan 9	13.80	12.58	11.47
8	Gaia21ebu	2024 Jan 9	13.05	12.05	11.54
9	Gaia21aul	2023 Jun 4	10.00	8.82	7.73
10	Gaia23bab	2024 Apr 11	14.11	12.93	12.29
11	Gaia23dhi	2024 Jun 10	14.79	13.47	12.56
13	Gaia21faq	2023 Jun 4	13.90	12.05	10.22
16	Gaia21csu	2024 Jan 9	13.17	12.15	11.70

Note. Errors are within 0.2 mag.

Appendix C
LBT Spectra

Here we show the optical and near-IR spectra of the sources of our sample. Quiescence, intermediate, and burst spectra are colored in red, green, and blue, respectively. Observation dates are indicated. Black stars are the photometric points obtained on the same night as the spectrum. The most important lines detected are labeled.

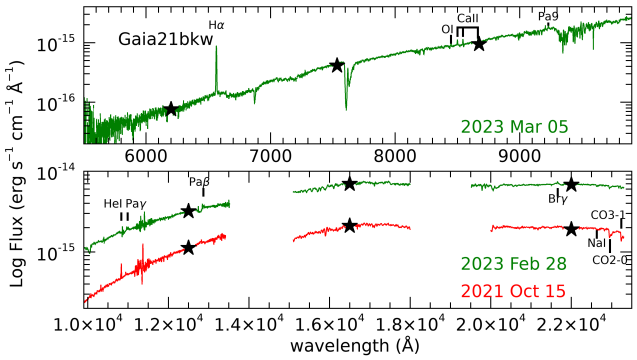

Figure 18. Quiescence and intermediate state spectrum of Gaia21bkw.

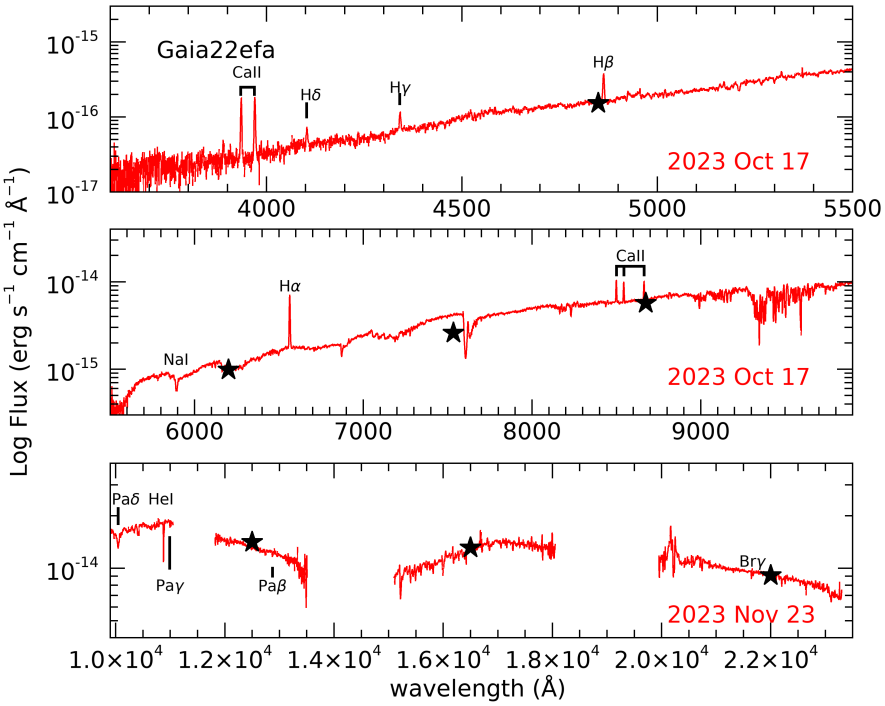

Figure 19. Quiescence spectrum of Gaia22efa.

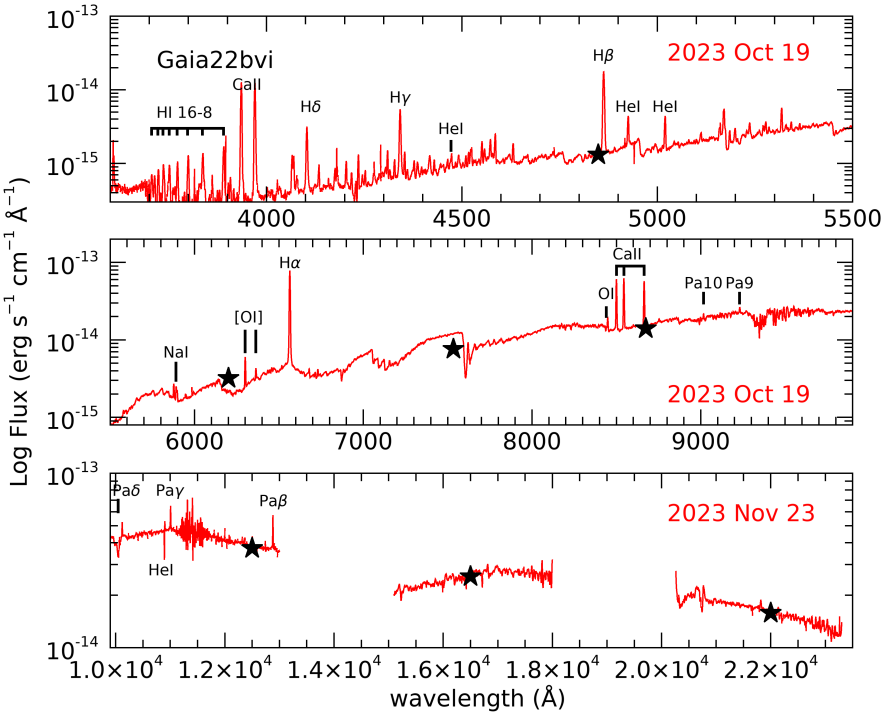

Figure 20. Quiescence spectrum of Gaia22bvi.

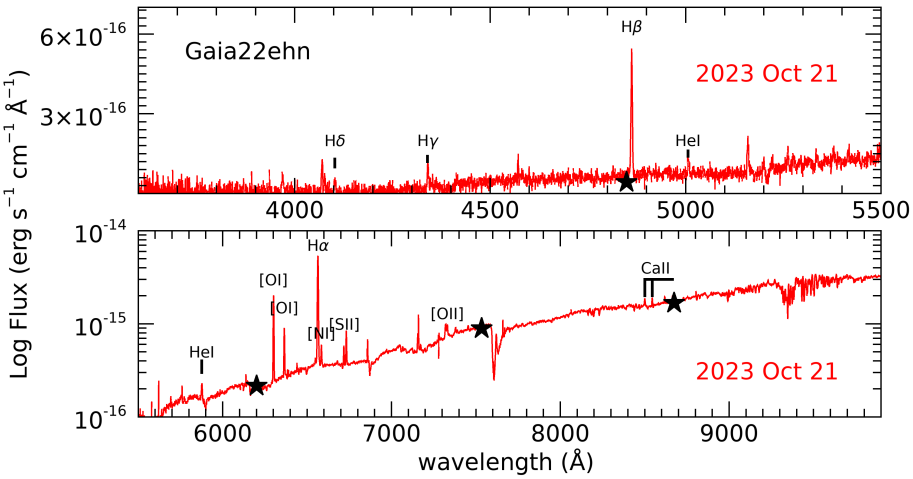

Figure 21. Quiescence spectrum of Gaia22ehn.

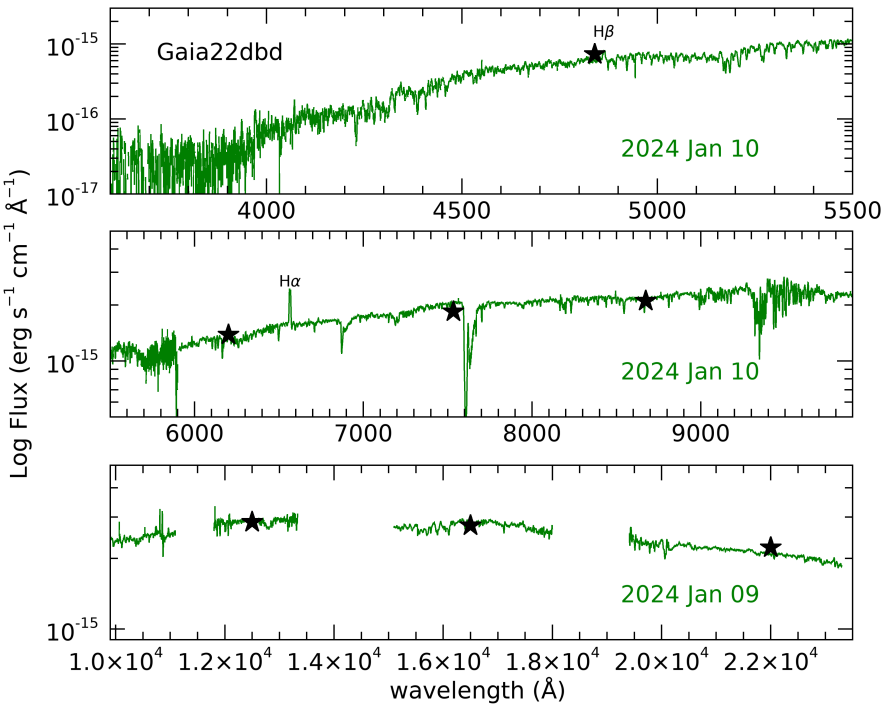

Figure 22. Intermediate state spectrum of Gaia22dbd.

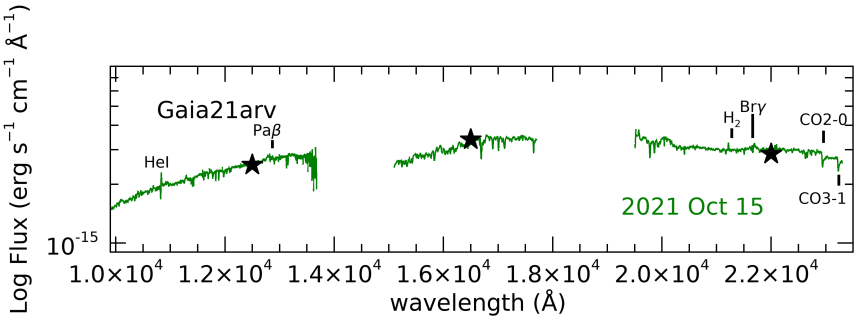

Figure 23. Intermediate state spectrum of Gaia21arv.

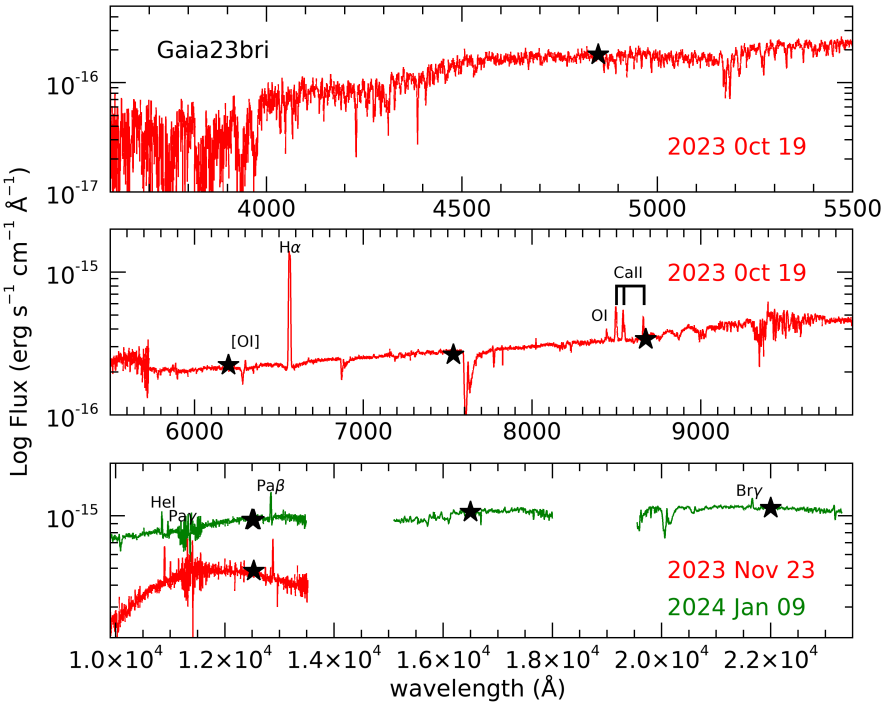

Figure 24. Quiescence and intermediate state spectrum of Gaia23bri.

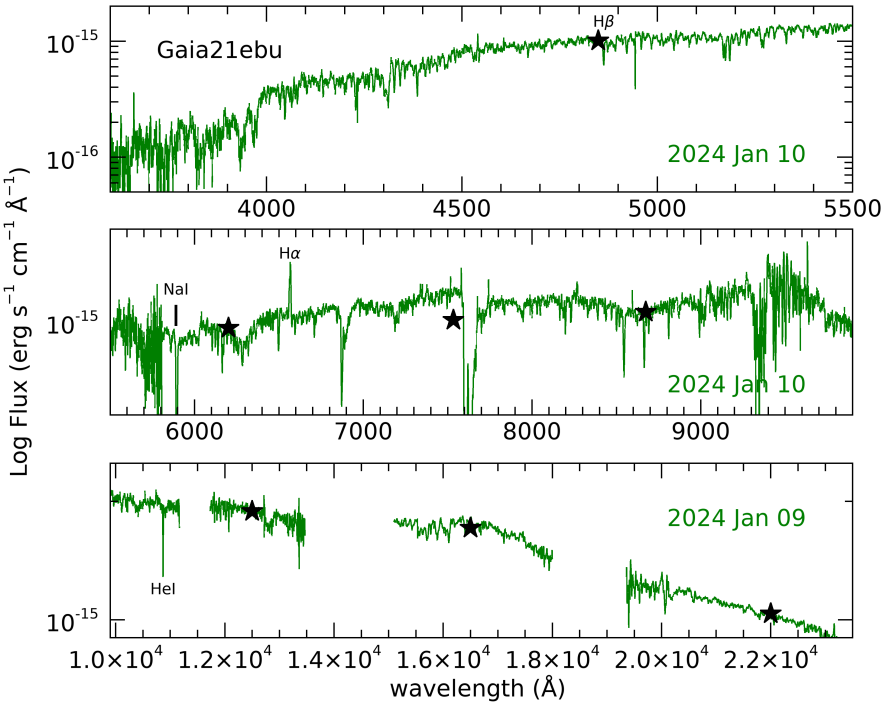

Figure 25. Intermediate state spectrum of Gaia21ebu.

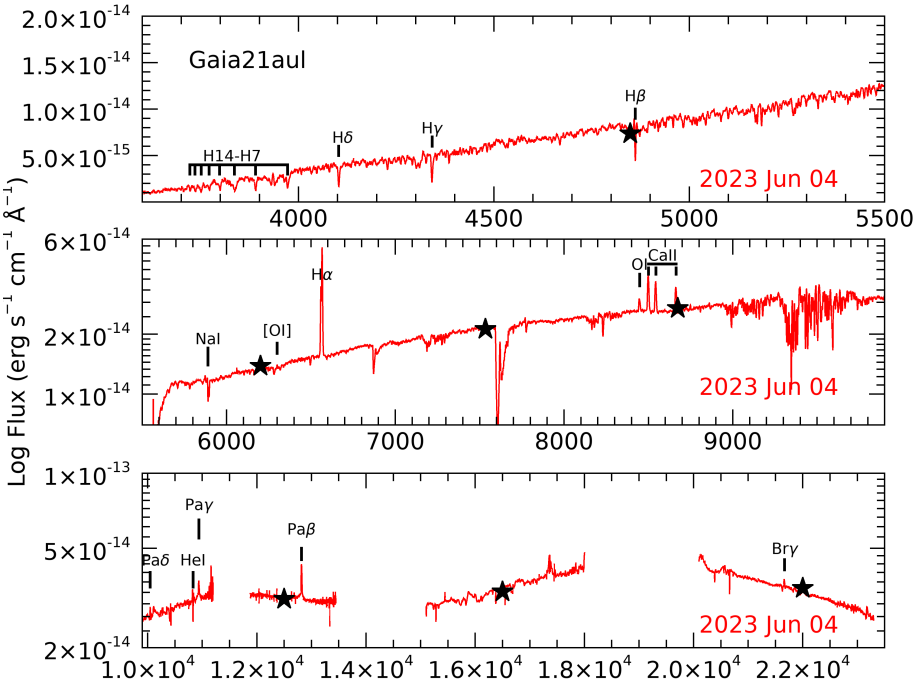

Figure 26. Quiescence spectrum of Gaia21aul.

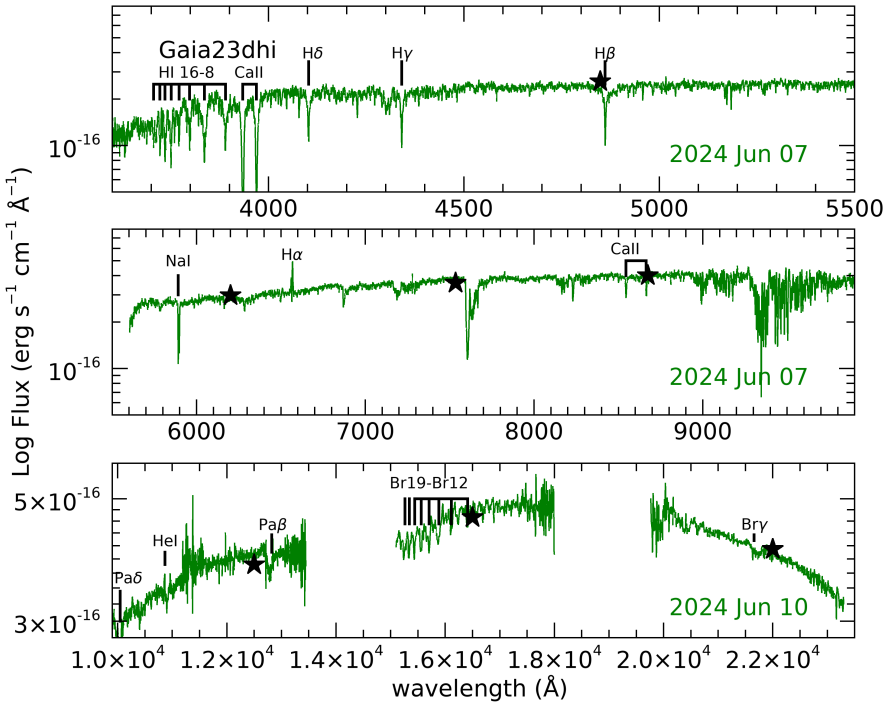

Figure 27. Intermediate state spectrum of Gaia23dhi.

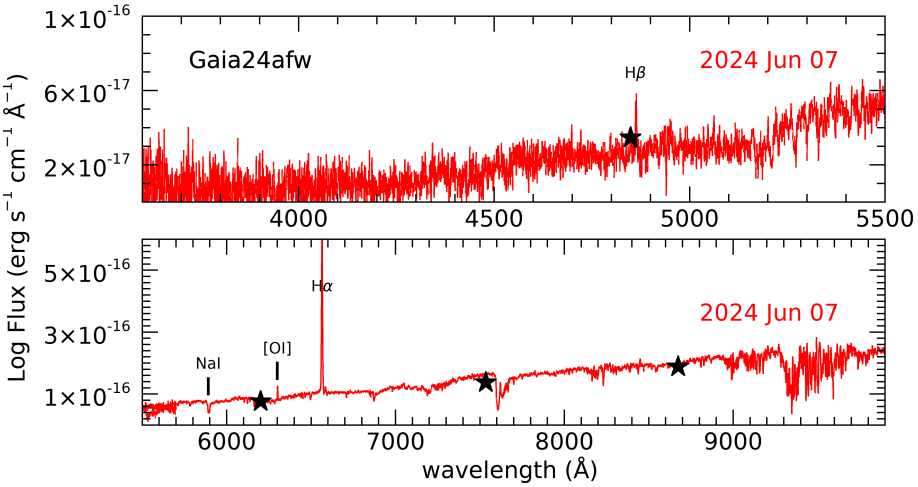

Figure 28. Quiescence spectrum of Gaia24afw.

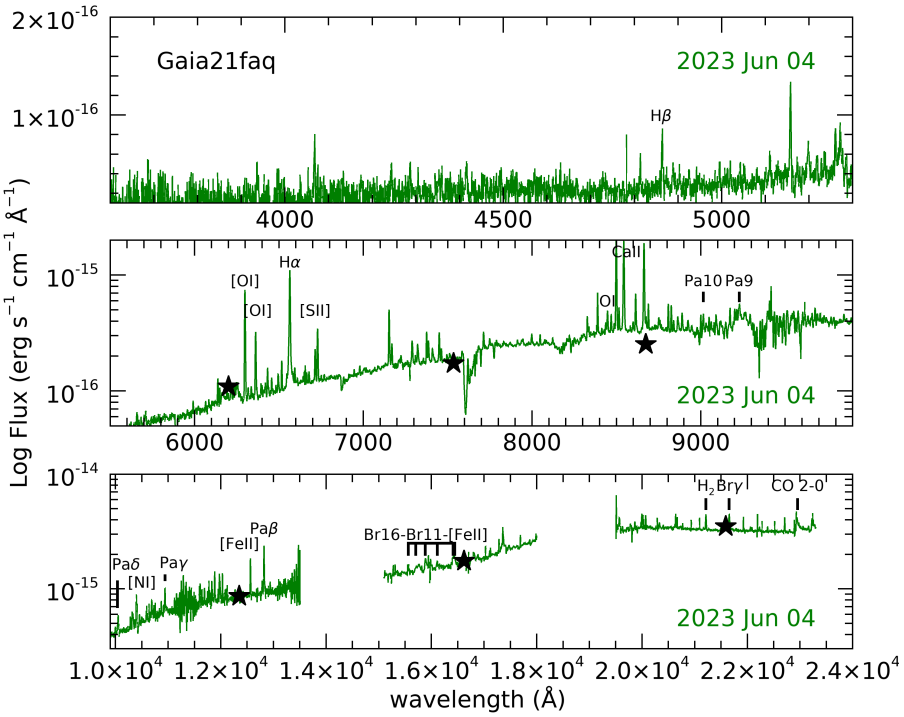

Figure 29. Intermediate state spectrum of Gaia21faq.

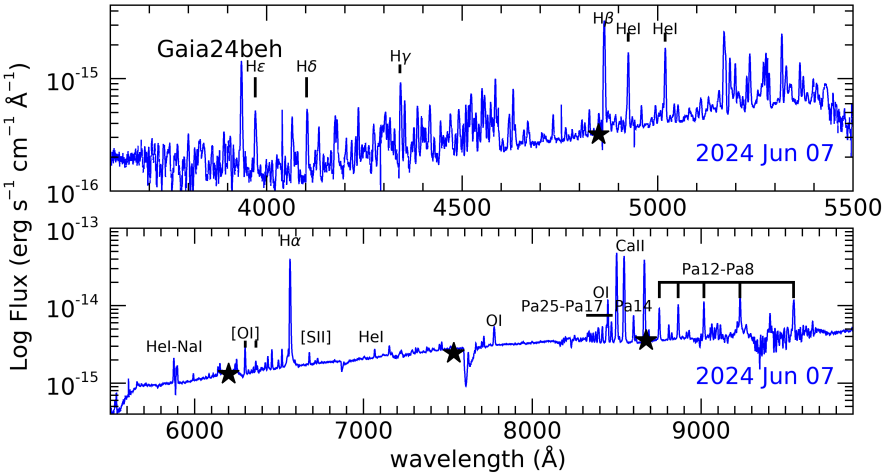

Figure 30. Burst spectrum of Gaia24beh.

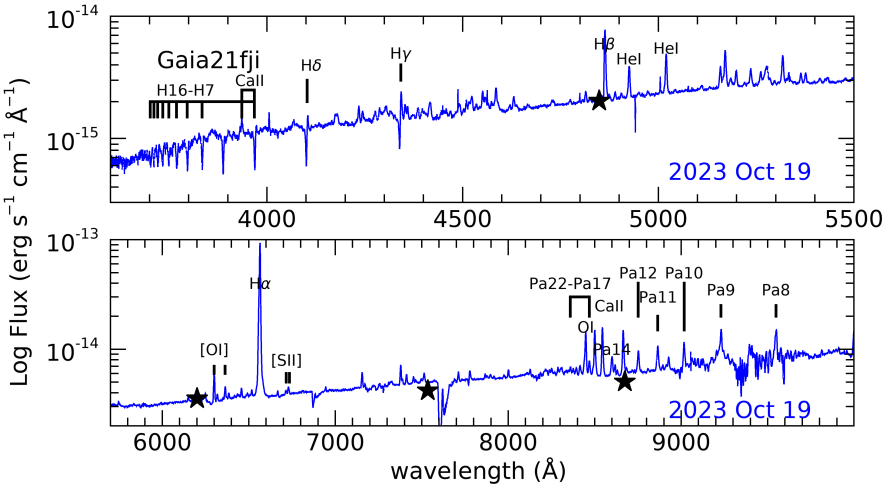

Figure 31. Burst spectrum of Gaia21fji.

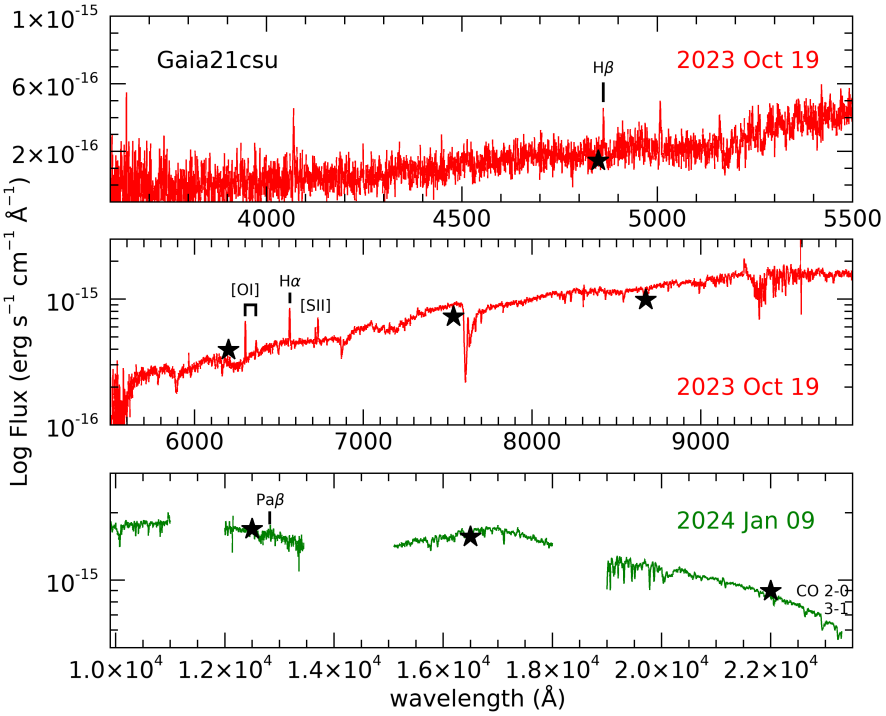

Figure 32. Quiescence and intermediate spectrum of Gaia21csu.

Appendix D
Line Fluxes

In this Appendix, we report the fluxes of Hydrogen (Table 10) and other accretion lines (Table 11), as well as fluxes of ejection lines (Table 12).

Table 10
Fluxes of Main Hydrogen Lines

Source	Date	Hδ	Hγ	Hβ	Hα	Paδ	Paγ	Paβ	Brγ
					F $\pm$ ΔF (10^{-16} erg s^{-1} cm^{-2})				
Gaia21bkw	2021 Oct 15	⋯	⋯	⋯	⋯	⋯	5 $\pm$ 2	11.3 $\pm$ 3.2	⋯
	2023 Feb 28	⋯	⋯	⋯	⋯	⋯	17.2 $\pm$ 1.9	65.3 $\pm$ 3.2	86.8 $\pm$ 4.1
	2023 Mar 5	⋯	⋯	⋯	46.7 $\pm$ 0.4	⋯	⋯	⋯	⋯
Gaia22efa	2023 Oct 17	1.7 $\pm$ 0.14	2.2 $\pm$ 0.14	9.4 $\pm$ 0.1	318 $\pm$ 0.2	⋯	⋯	⋯	⋯
Gaia22efa	2023 Nov 23	⋯	⋯	⋯	⋯	−940 $\pm$ 49	−150 $\pm$ 49	−105 $\pm$ 38	−102 $\pm$ 47
Gaia22bvi	2023 Oct 19	105.6 $\pm$ 1.1	189.1 $\pm$ 1.4	713.9 $\pm$ 1.1	4736 $\pm$ 1.8	⋯	⋯	⋯	⋯
	2023 Nov 23	⋯	⋯	⋯	⋯	−2320 $\pm$ 160	488.6 $\pm$ 130	1729 $\pm$ 80	⋯
Gaia22ehn	2023 Oct 19	2.6 $\pm$ 0.4	4.1 $\pm$ 0.3	19.6 $\pm$ 0.2	288.0 $\pm$ 0.5	⋯	⋯	⋯	⋯
Gaia22dbd	2024 Jan 10	⋯	⋯	13.5 $\pm$ 1.2	96.8 $\pm$ 1.2	⋯	⋯	⋯	⋯
Gaia21arv	2021 Oct 15	⋯	⋯	⋯	⋯	⋯	⋯	17.2 $\pm$ 4.6	66.3 $\pm$ 11
Gaia23bri	2023 Oct 19	⋯	⋯	⋯	140.1 $\pm$ 0.9	⋯	⋯	⋯	⋯
	2023 Nov 23	⋯	⋯	⋯	⋯	⋯	14.1 $\pm$ 1.7	44.6 $\pm$ 1.7	⋯
	2024 Jan 9	⋯	⋯	⋯	⋯	⋯	23.6 $\pm$ 1.7	78.3 $\pm$ 2.0	40.5 $\pm$ 3
Gaia21ebu	2024 Jan 10	⋯	⋯	−12.5 $\pm$ 1.0	31.8 $\pm$ 0.5	⋯	⋯	⋯	⋯
Gaia21aul	2023 Jun 4	−108 $\pm$ 10	−104 $\pm$ 7.4	−95.5 $\pm$ 8.8	2429 $\pm$ 22	−852 $\pm$ 70	907 $\pm$ 43	2565 $\pm$ 88	(−224) 442 $\pm$ 110
Gaia23bab	2024 Apr 11	⋯	⋯	⋯	25.7 $\pm$ 0.1	7.8 $\pm$ 1.1	13.0 $\pm$ 1.0	13.1 $\pm$ 1.0	9.1 $\pm$ 2.3
Gaia23dhi	2024 Jun 7	−6.1 $\pm$ 0.1	−5.2 $\pm$ 0.1	−7.5 $\pm$ 0.1	3.1 $\pm$ 0.1	−33.4 $\pm$ 0.1		−27 $\pm$ 0.1	−4.0 $\pm$ 0.1
Gaia24afw	2024 Jun 7	⋯	⋯	1.1 $\pm$ 0.4	36.9 $\pm$ 0.1	⋯	⋯	⋯	⋯
Gaia21faq	2023 Jun 4	⋯	⋯	1.6 $\pm$ 0.4	65.8 $\pm$ 0.6	34.1 $\pm$ 1.9	47.7 $\pm$ 1.2	172.6 $\pm$ 1.4	282.0 $\pm$ 2.3
Gaia24beh	2024 Jun 7	17.8 $\pm$ 0.4	33.6 $\pm$ 0.4	132.7 $\pm$ 0.4	2631 $\pm$ 1.1	⋯	⋯	⋯	⋯
Gaia21fji	2023 Oct 19	(−18) 9.6 $\pm$ 1.7	(−44) 28.5 $\pm$ 1.6	236 $\pm$ 1.6	7047 $\pm$ 3.3	⋯	⋯	⋯	⋯
Gaia21csu	2023 Oct 19	⋯	⋯	6.4 $\pm$ 0.5	26.9 $\pm$ 1.0	⋯	⋯	⋯	⋯
	2024 Jan 9	⋯	⋯	⋯	⋯	⋯	⋯	16.2 $\pm$ 2.4	⋯

Note. Negative numbers in parentheses represent fluxes of absorption components.

Table 11
Fluxes of Other Accretion Lines

Source	Date	OI 8448	HeI 4925	HeI 5020	HeI 5876	CaII 8500	CaII 8544	CaII 8664
					F ± ΔF (10^{-16} erg s^{-1} cm^{-2})			
Gaia21bkw	2023 Mar 5	6.7 ± 0.4	⋯	⋯	⋯	11.5 ± 0.4	9.9 ± 0.4	8.8 ± 0.5
Gaia22efa	2023 Oct 17	⋯	⋯	⋯	⋯	237 ± 0.2	219 ± 0.2	203 ± 0.2
Gaia22bvi	2023 Oct 19	257.3 ± 1.7	95.6 ± 1.1	96.6 ± 1.0	46.2 ± 1.8	2576 ± 1.6	2767 ± 2.0	2415 ± 1.8
Gaia22ehn	2023 Oct 19	⋯	⋯	⋯	4.6 ± 0.7	22.1 ± 0.7	15.5 ± 0.6	15.8 ± 0.5
Gaia23bri	2023 Oct 19	6.1 ± 0.4	⋯	⋯	⋯	24.5 ± 0.6	19.6 ± 0.7	12.9 ± 0.6
Gaia21aul	2023 Jun 4	402 ± 19	⋯	⋯	⋯	1230 ± 18	978 ± 22	771 ± 19
Gaia23bab	2024 Apr 11	2.9 ± 0.1	⋯	⋯	1.1 ± 0.1	2.5 ± 0.1	2.4 ± 0.1	2.2 ± 0.1
Gaia23dhi	2024 Jun 10	⋯	⋯	⋯	⋯	⋯	−6.8 ± 0.1	−3.9 ± 0.1
Gaia21faq	2023 Jun 4	10.7 ± 0.6	⋯	⋯	⋯	107 ± 0.6	104 ± 0.5	94 ± 0.5
Gaia24beh	2024 Jun 7	519.8 ± 0.6	55.8 ± 0.4	57.7 ± 0.4	65.9 ± 0.5	2886 ± 0.7	2947 ± 0.7	2538 ± 0.7
Gaia21fji	2023 Oct 19	744.2 ± 3.3	84.6 ± 1.8	112.3 ± 1.9		76.7 ± 2.4	84.2 ± 3.0	81.4 ± 3.2

Note. Negative numbers in parentheses represent fluxes of absorption components.

Table 12
Fluxes of Main Ejection Lines

Source	Date	He I 1.08	[O I] 6300	[S II] 6732	[N I] 1.04	[N II] 6584	[Fe II] 1.25	H_2 2.12
				$F \pm \Delta F$ (10^{-16} erg s^{-1} cm^{-2})				
Gaia21bkw	2021 Oct 15	24.0 ± 1.8	⋯	⋯	⋯	⋯	⋯	⋯
⋯	2023 Feb 28	(−8) 26.0 ± 1.6	⋯	⋯	⋯	⋯	⋯	⋯
Gaia22efa	2023 Nov 23	−721 ± 39	⋯	⋯	⋯	⋯	⋯	⋯
Gaia22bvi	2023 Oct 19	⋯	190.5 ± 1.7	⋯	⋯	⋯	⋯	⋯
⋯	2023 Nov 23	−933 ± 67	⋯	⋯	⋯	⋯	⋯	⋯
Gaia22ehn	2023 Oct 19	⋯	83.9 ± 0.6	20.4 ± 0.6	⋯	11.0 ± 0.6	⋯	⋯
Gaia21arv	2021 Oct 15	(−24.3) 33.5 ± 4.1	⋯	⋯	⋯	⋯	⋯	35.1 ± 0.6
Gaia23bri	2023 Oct 19	⋯	2.2 ± 0.4	⋯	⋯	⋯	⋯	⋯
⋯	2023 Nov 23	37.2 ± 1.3	⋯	⋯	⋯	⋯	⋯	⋯
⋯	2024 Jan 9	37.9 ± 1.7	⋯	⋯	⋯	⋯	⋯	⋯
Gaia21ebu	2024 Jan 9	−51.2 ± 1.1	⋯	⋯	⋯	⋯	⋯	⋯
Gaia21aul	2023 Jun 4	(−53.9) 16.7 ± 43	24.7 ± 18	⋯	⋯	⋯	⋯	⋯
Gaia23bab	2024 Apr 11	11.4 ± 1.0	0.5 ± 0.1	⋯	⋯	⋯	⋯	⋯
Gaia23dhi	2024 Jun 7	−33.4 ± 9.1	⋯	⋯	⋯	⋯	⋯	⋯
Gaia24afw	2024 Jun 7	⋯	1.5 ± 0.1	⋯	⋯	⋯	⋯	⋯
Gaia21faq	2023 Jun 4	⋯	35.6 ± 0.5	11.7 ± 0.5	71.2 ± 1.8	⋯	96.5 ± 1.2	184.5 ± 2.5
Gaia24beh	2024 Jun 7	⋯	94.7 ± 0.6	17.8 ± 0.7	⋯	⋯	⋯	⋯
Gaia21fji	2023 Oct 19	⋯	198.2 ± 2.8	56.0 ± 3.3	⋯	⋯	⋯	⋯
Gaia21csu	2023 Oct 19	⋯	19.4 ± 1.1	13.8 ± 0.9	⋯	⋯	⋯	⋯

Note. Negative numbers in parentheses represent fluxes of absorption components.

ORCID iDs

Teresa Giannini https://orcid.org/0000-0002-7035-8513
Manuele Gangi https://orcid.org/0000-0002-8364-7795
Fernando Cruz-Sáenz de Miera https://orcid.org/0000-0002-4283-2185
Brunella Nisini https://orcid.org/0000-0002-9190-0113
Máté Szilágyi https://orcid.org/0000-0002-3648-433X
Katia Biazzo https://orcid.org/0000-0002-1892-2180
Ágnes Kóspál https://orcid.org/0000-0001-7157-6275
Péter Ábrahám https://orcid.org/0000-0001-6015-646X
Simone Antoniucci https://orcid.org/0000-0002-0666-3847
Roberta Carini https://orcid.org/0000-0003-1604-2064
Eleonora Fiorellino https://orcid.org/0000-0002-5261-6216
Adriana Gargiulo https://orcid.org/0000-0002-3351-1216
Ester Marini https://orcid.org/0000-0002-6894-1267
Zsófia Nagy https://orcid.org/0000-0002-3632-1194
Maria Gabriela Navarro https://orcid.org/0000-0002-1860-2304
Fabrizio Vitali https://orcid.org/0000-0001-8332-4227

References

Alcalá, J. M., Manara, C. F., Natta, A., et al. 2017, A&A, 600, A20
Alcalá, J. M., Natta, A., Manara, C. F., et al. 2014, A&A, 561, A2
Aspin, C., & Reipurth, B. 2003, AJ, 126, 2936
Audard, M., Ábrahám, P., Dunham, M. M., et al. 2014, in Protostars and Planets VI, ed. H. Beuther, R. S. Klessen, C. P. Dullemond, & T. Henning (Univ. Arizona Press), 387
Bae, J., Hartmann, L., Zhu, Z., et al. 2014, ApJ, 795, 61
Bailer-Jones, C. A. L., Rybizki, J., Fouesneau, M., et al. 2021, AJ, 161, 147
Bell, K. R., & Lin, D. N. C. 1994, ApJ, 427, 987
Bellm, E. C., Kulkarni, S. R., Graham, M. J., et al. 2019, PASP, 131, 018002
Bonnell, I., & Bastien, P. 1992, ApJL, 401, L31
Borchert, E. M. A., Price, D. J., Pinte, C., et al. 2022, MNRAS, 517, 4436

Bouvier, J., Alencar, S. H. P., Boutelier, T., et al. 2007, A&A, 463, 1017
Caratti o Garatti, A., Stecklum, B., Garcia Lopez, R., et al. 2017, NatPh, 13, 276
Cardelli, J. A., Clayton, G. C., & Mathis, J. S. 1989, ApJ, 345, 245
Chambers, K. C., Magnier, E. A., Metcalfe, N., et al. 2016, arXiv:1612.05560
Connelley, M. S., & Reipurth, B. 2018, ApJ, 861, 145
Contreras-Peña, C., Lee, J.-E., Herczeg, G., et al. 2025b, JKAS, 58, 209
Contreras-Peña, C., Lee, J.-E., Lee, H.-G., et al. 2025a, ApJ, 987, 23
Cruz-Sáenz de Miera, F., Kóspál, Á., Ábrahám, P., et al. 2022, ApJ, 927, 125
Cruz-Sáenz de Miera, F., Kóspál, Á., Abrahám, P., et al. 2023, A&A, 678, A88
Cutri, R. M., Mainzer, A., Conrow, T., et al. 2015, Explanatory Supplement to the NEOWISE Data Release Products,
Dahm, S. E., & Hillenbrand, L. A. 2020, AJ, 160, 278
Dong, R., Liu, H. B., Cuello, N., et al. 2022, NatAs, 6, 331
Dullemond, C. P., Küffmeier, M., Goicovic, F., et al. 2019, A&A, 628, A20
Edenhofer, G., Zucker, C., Frank, P., et al. 2024, A&A, 685, A82
Fiorellino, E., Ábrahám, P., Kóspál, Á., et al. 2024, A&A, 686, A160
Fiorellino, E., Manara, C. F., Nisini, B., et al. 2021, A&A, 650, A43
Fischer, W. J., Hillenbrand, L. A., Herczeg, G. J., et al. 2023, ASPC, 534, 355
Fischer, W. J., Safron, E., & Megeath, S. T. 2019, ApJ, 872, 183
Gaia Collaboration, Prusti, T., de Bruijne, J. H. J., et al. 2016, A&A, 595, A1
Gargiulo, A., Fumana, M., Bisogni, S., et al. 2022, MNRAS, 514, 2902
Giannini, T., Giunta, A., Gangi, M., et al. 2022, ApJ, 929, 129
Giannini, T., Schisano, E., Nisini, B., et al. 2024, ApJ, 967, 41
Ghosh, A., Sharma, S., Ninan, J. P., et al. 2022, ApJ, 926, 68
Green, G. M. 2018, JOSS, 3, 695
Green, G. M., Schlafly, E., Zucker, C., et al. 2019, ApJ, 887, 93
Greene, T. P., & Lada, C. J. 1996, AJ, 112, 2184
Großschedl, J. E., Alves, J., Teixeira, P. S., et al. 2019, A&A, 622, A149
Gullbring, E., Hartmann, L., Briceño, C., et al. 1998, ApJ, 492, 323
Jayasinghe, T., Kochanek, C. S., Stanek, K. Z., et al. 2018, MNRAS, 477, 3145
Hartmann, L., Calvet, N., Gullbring, E., et al. 1998, ApJ, 495, 385
Hartmann, L., & Kenyon, S. J. 1996, ARA&A, 34, 207
Herbig, G. H. 1977, ApJ, 217, 693
Herbig, G. H. 1989, ESOC, 33, 233
Hernández, J., Calvet, N., Hartmann, L., et al. 2005, AJ, 129, 856
Hillenbrand, L. A., Contreras-Peña, C., Morrell, S., et al. 2018, ApJ, 869, 146
Hillenbrand, L. A., Reipurth, B., Connelley, M., et al. 2019, AJ, 158, 240
Hodapp, K. W., Denneau, L., Tucker, M., et al. 2020, AJ, 160, 164
Hodapp, K. W., Reipurth, B., Pettersson, B., et al. 2019, AJ, 158, 241
Hodgkin, S. T., Harrison, D. L., Breedt, E., et al. 2021, A&A, 652, A76
Hubbard, A. 2017, MNRAS, 465, 1910
Hunt, E. L., & Reffert, S. 2024, A&A, 686, A42
Hunter, T. R., Brogan, C. L., MacLeod, G., et al. 2017, SMAN, 24, 2
Kadam, K., Vorobyov, E., Regály, Z., et al. 2020, ApJ, 895, 41
Kennedy, G. M., Kenworthy, M. A., Pepper, J., et al. 2017, RSOS, 4, 160652
Kounkel, M., Covey, K., Moe, M., et al. 2019, AJ, 157, 196
Kraus, A. L., & Hillenbrand, L. A. 2007, AJ, 134, 2340
Lee, Y.-H., Johnstone, D., Lee, J.-E., et al. 2021, ApJ, 920, 119
Lodato, G., & Clarke, C. J. 2004, MNRAS, 353, 841
Lorenzetti, D., Giannini, T., Larionov, V. M., et al. 2007, ApJ, 665, 1182
Mamajek, E. E., Barenfeld, S. A., Ivanov, V. D., et al. 2015, ApJL, 800, L17
Mainzer, A., Bauer, J., Grav, T., et al. 2011, ApJ, 731, 53
Manara, C. F., Frasca, A., Venuti, L., et al. 2021, A&A, 650, A196
Marton, G., Abraham, P., Szegedi-Elek, E., et al. 2019, yCat. , 2360 II/360
Megeath, S. T., Gutermuth, R., Muzerolle, J., et al. 2012, AJ, 144, 192
Meyer, M. R., Calvet, N., & Hillenbrand, L. A. 1997, AJ, 114, 288
Minniti, D., Lucas, P. W., Emerson, J. P., et al. 2010, NewA, 15, 433
Murakami, H., Baba, H., Barthel, P., et al. 2007, PASJ, 59, S369
Nagy, Z., Kóspál, Á., Ábrahám, P., et al. 2025, ApJ, 987, 37
Nagy, Z., Park, S., Ábrahám, P., et al. 2023, MNRAS, 524, 3344
Nayakshin, S., Cruz Sáenz de Miera, F., Kóspál, Á., et al. 2024, MNRAS, 530, 1749
Nayakshin, S., Owen, J. E., & Elbakyan, V. 2023, MNRAS, 523, 385
Park, S., Kóspál, Á., Ábrahám, P., et al. 2022, ApJ, 941, 165
Pecaut, M. J., & Mamajek, E. E. 2013, ApJS, 208, 9
Pogge, R. W., Atwood, B., Brewer, D. F., et al. 2010, SPIE, 7735, 77350A
Rieke, G. H., Young, E. T., Engelbracht, C. W., et al. 2004, ApJS, 154, 25
Safron, E. J., Fischer, W. J., Megeath, S. T., et al. 2015, ApJL, 800, L5
Seifert, W., Appenzeller, I., Baumeister, H., et al. 2003, SPIE, 4841, 962
Siess, L., Dufour, E., & Forestini, M. 2000, A&A, 358, 593
Siwak, M., Hillenbrand, L. A., Kóspál, Á., et al. 2023, MNRAS, 524, 5548
Skrutskie, M. F., Cutri, R. M., Stiening, R., et al. 2006, AJ, 131, 1163
Szegedi-Elek, E., Ábrahám, P., Wyrzykowski, Ł., et al. 2020, ApJ, 899, 130
Tripicchio, A., Severino, G., Covino, E., et al. 1997, A&A, 327, 681
Venuti, L., Bouvier, J., Flaccomio, E., et al. 2014, A&A, 570, A82
Venuti, L., Bouvier, J., Irwin, J., et al. 2015, A&A, 581, A66
Vorobyov, E. I., & Basu, S. 2015, ApJ, 805, 115
Wichittanakom, C., Oudmaijer, R. D., Fairlamb, J. R., et al. 2020, MNRAS, 493, 234
Wright, E. L., Eisenhardt, P. R. M., Mainzer, A. K., et al. 2010, AJ, 140, 1868
Zakri, W., Megeath, S. T., Fischer, W. J., et al. 2022, ApJL, 924, L23
Zhu, Z., Hartmann, L., Gammie, C., et al. 2009, ApJ, 701, 620